Geoscience Frontiers 10 (2019) 2117–2133

HOSTED BY

Contents lists available at ScienceDirect

China University of Geosciences (Beijing)

Geoscience Frontiers

journal homepage: www.elsevier.com/locate/gsf

Research Paper

Geomechanical model for a seismically active geothermal field: Insights from the Tinguiririca volcanic-hydrothermal system

L. Giambiagi [a,*], P. Álvarez [b], S. Spagnotto [c], E. Godoy [b], A. Lossada [d], J. Mescua [a,e], M. Barrionuevo [a], J. Suriano [a]

[a] IANIGLA, CCT Mendoza, CONICET, Parque San Martín s/n, 5500, Mendoza, Argentina
[b] TEHEMA S.A., Subercaseaux 4100, Pirque, Chile
[c] Universidad Nacional de San Luis, Consejo Nacional de Investigaciones Científicas y Técnicas, Argentina
[d] Universidad de Buenos Aires, Consejo Nacional de Investigaciones Científicas y Técnicas, Instituto de Estudios Andinos (IDEAN), Facultad de Ciencias Exactas y Naturales, Buenos Aires, Argentina
[e] Facultad de Ciencias Exactas y Naturales, Universidad Nacional de Cuyo, Argentina

ARTICLE INFO

Article history:
Received 20 July 2018
Received in revised form
17 January 2019
Accepted 27 February 2019
Available online 12 April 2019

Keywords:
Southern central Andes
Paleostress analysis
Fluid migration
Coulomb static stress change

ABSTRACT

In this work, we develop a multidisciplinary approach to investigate a geothermal system located at the volcanic arc of a subduction-related orogen and highlight the interplay between active tectonism, stress field and fluid migration. By using results of field investigations from the Tinguiririca geothermal field in the High Andes of Chile (35°S), empirical analysis, and numerical models of static stress variations, we proposed a geomechanical model for evaluating the distribution of hydrothermal manifestations in a seismically-active region. The present geomechanical model follows four major steps: (1) development of the 3D structural model of fault pattern; (2) estimation of the *in-situ* stress field; (3) calculation of the resolved-shear-to-normal-stress ratio (slip tendency) on each fault with varying geomechanical parameters (coefficient of friction, pore pressure and cohesion) as inputs; and (4) estimation of Coulomb static stress changes as a consequence of failure in a nearby fault. Through combination of all these analyses, we characterize in detail both the active deformation in the geothermal field and its relationship with hot fluid migration.

1. Introduction

Fracturing and faulting processes play a fundamental role in the transport and migration of fluids, controlling the distribution of magmas, hydrocarbon fields and hydrothermal fluids. Reciprocally, the presence and migration of fluids have a main impact on the stress state of faults and on mechanical failure (Hubbert and Rubey, 1959; Sibson, 1977), as well as the chemical properties inside faults and fractures (Faulkner et al., 2010). However, not all fault and fractures contribute to the migration of fluids. Their orientation and spatial distribution, with respect to the *in-situ* stress field and fluid pressure, define which faults are prone to slip and which ones to remain stable (Morris et al., 1996). Critically stressed faults for frictional failure, or potentially active faults on the verge of failure, are regarded as being effective fluid conduits (Barton et al., 1995; Sibson, 1996; Tezuka and Niitsuma, 2000; Townend and Zoback, 2000; Moeck et al., 2009). The stress state of faults may therefore serve as a quantitative proxy for permeability at scales of hundreds of meters (Siler et al., 2015).

While normal stresses (σ_n) acting on faults and fractures tend to reduce their aperture, and inhibit fluid migration, tangential stresses (τ) promote dilation and favour fluid circulation (Aydin, 2000). Critically stressed faults are those optimally oriented with respect to the *in-situ* stress field, with a ratio of shear to normal stress (τ/σ_n) close to the critical value of failure, which in turn is governed by the frictional coefficient μ (Byerlee, 1978; Jaeger and Cook, 1979). Accordingly, low values of normal stress, as well as high differential stress ($\sigma_1-\sigma_3$) and high fluid pressure, create anisotropic permeability patterns which focalize fluid migration (Barton et al., 1995). Other factors controlling the upwelling of geothermal fluids include: the presence of fault intersections, step-overs, and fault tips (Curewitz and Karson, 1997; Marten and Boger,

* Corresponding author.
E-mail address: palvarez@tehema.cl (L. Giambiagi).
Peer-review under responsibility of China University of Geosciences (Beijing).

https://doi.org/10.1016/j.gsf.2019.02.006

1998; Sibson and Rowland, 2003), as well as stresses generated by earthquakes and then transferred to structures near the hypocenter (Micklethwaite and Cox, 2006; Siler et al., 2015). Therefore, an accurate interpretation of a geothermal system in areas of active tectonism depends on the reliability of a geomechanical model that considers the resolved stresses on each fault of the structural system, and coseismic static stress change produced by local earthquakes.

In geothermal fields, the critical failure state of faults can be explained by elevated pore fluid pressure, which reduces rock strength (Hill et al., 1993). In fields located in seismically active areas, the combined effect of static stress changes from mainshocks and clusters of smaller earthquakes can be correlated with large, fracture-related, fluid flux (Micklethwaite and Cox, 2006; Sheldon and Micklethwaite, 2007). Few-bar static stress variations may reduce the confining pressure on the magma chamber (Wicks et al., 2011), promoting its pressurisation (Druitt et al., 2012). Fluid injection from the pressurised magmatic chamber during these coseismic events decreases the effective normal stress, resulting in fracture dilation (Walsh and Grosenbaugh, 1979; Sibson, 1990) or shear on favourable oriented faults (Tezuka and Niitsuma, 2000; Lupi and Miller, 2014). The unclamping process (reduction of σ_n acting on the fault) may trigger fault rupture and induce transient permeability along fault planes and associated fracture networks (Rowland and Sibson, 2004; Cox, 2005). According to Curewitz and Karson (1997), the distribution of geothermal activity is related to permeability maintenance mechanisms, which are fracturing due to stress concentration (dynamic maintenance) and fracturing due to fault slip (kinematic maintenance), the former being the more important.

The geothermal fields in the Southern Volcanic Zone between 34.5°S and 36°S provide a natural laboratory for the study of the structural control on the geothermal system and its relationship with short-term stress field variations due to local earthquakes. The most outstanding feature in this area is the existence of a NNE volcanic arc alignment (Arcos, 1987; Lavenu and Cembrano, 1999; Cembrano and Lara, 2009; Bonali et al., 2013), where most of the crustal seismic activity is concentrated (PDE catalog, Lira, 2011; Villegas et al., 2016), as can be shown from the distribution of focal mechanisms (Fig. 1A; CMT catalog, Alvarado et al., 2005; Spagnotto et al., 2015; Villegas et al., 2016). Most of the reported focal mechanisms (CMT; Alvarado et al., 2005; Spagnotto et al., 2015; Villegas et al., 2016) are strike-slip ones with no-or-minor dip-slip component. A main earthquake occurred on August 28, 2004, (M_w 6.5, CMT catalog) in the Tinguiririca area. The highest reported intensities of this earthquake occurred in the study region (Fig. 2).

The Tinguiririca geothermal project is located in the High Andes at 34°50'S, in the western flank of the Tinguiririca volcanic complex (Clavero et al., 2011). This complex is composed of three volcanic edifices: Tinguiririca, Montserrat and Fray Carlos, all aligned in a NNE direction (Arcos, 1987) and subparallel to the main faults of the area (Fig. 3). Thermal activity in the study area is distributed in four hydrothermal areas: Los Azufres, Los Humos, Las Choicas and Termas del Flaco (Clavero et al., 2011). Geochemical characteristics indicate the presence of an active magmatic system underlying the hydrothermal system (Benavente et al., 2012; Benavente, 2015).

In this paper, we investigate the control of *in-situ* stress magnitude and orientation over the reactivation of pre-existing faults, and we explore the effect that stress-transfer due to local earthquakes may have on static stress changes on the main active faults affecting the geothermal field. The main goals of this research are to determine the areas with the highest potential to be fluid migration conducts, and to investigate the relationship between fault stress state, seismic activity in neighbouring faults and fluid circulation.

2. Geological setting

The study area is situated in the northern part of the Southern Volcanic Zone (Fig. 1A). The arc region at these latitudes is characterized by a volcanic arc basement composed of Meso–Cenozoic volcano-sedimentary rocks, deformed into the Malargüe fold-and-thrust belt (Fig. 1B) and locally intruded by Mio–Pliocene plutons (Godoy et al., 1999; Charrier et al., 2002; Tapia and Farías, 2011; Mescua et al., 2013).

During the Late Triassic to Early Jurassic, extension along the western South American continental margin resulted in the Neuquén basin aperture (Vergani et al., 1995). At the study latitude, the Triassic–Jurassic Río del Cobre depocenter developed, filled with sedimentary and volcaniclastic rocks (Mescua et al., 2014). This depocenter is inferred to have been controlled by movement along a NNE-striking master fault, here called Río Damas fault (Fig. 1B), currently buried under the volcanic arc deposits.

The oldest outcrops in the study area correspond to the Upper Jurassic–Lower Cretaceous marine and continental sequences of the Neuquén basin. During the Late Cretaceous, continental red beds (95–80 Ma, U-Pb detrital zircon ages from Muñoz et al., 2018) registered the initial subsidence of an Andean foreland basin (Charrier et al., 1996) and a new compressional period (Iannelli et al., 2018; Muñoz et al., 2018). Previous detailed petrographic and geochronological analysis of the exposures in the volcanic arc area (Arcos, 1987; Arcos et al., 1988; Charrier et al., 1996; Pavez et al., 2016; Muñoz et al., 2018; Mosolf et al., 2018) describe the volcanic arc as composed of: (i) a thick succession of dacitic to rhyolitic tuffs, basalts, and andesites of Late Cretaceous age ($^{40}Ar/^{39}Ar$ age and U-Pb zircon ages spanning 62–74 Ma from Mosolf et al., 2018), grouped into the Guanaco volcanic unit by Tapia et al. (2015) or Plan de los Yueques Fm. by Pavez et al. (2016); (ii) basalt and andesite lavas, ignimbrites and lahar deposits of early to late Eocene age (37–52 Ma; Mosolf et al., 2018) interbedded with continental clastic and volcaniclastic rocks; (iii) a thick sequence of volcaniclastic deposits and acidic-to-intermediate lavas of the Abanico Formation, with ages ranging from late Eocene to lower late Miocene (37–16 Ma; Klohn, 1960; Charrier et al., 1996), interpreted as an intra-arc extensional basin (Godoy et al., 1999; Charrier et al., 2002); (iv) volcanic deposits of the Farellones Formation of late Miocene age (11–12 Ma; Aguirre et al., 2009); and (v) lower Pleistocene to Holocene volcanic centers aligned along a NNE strip (Arcos, 1987; Arcos et al., 1988; Charrier et al., 1996; Mosolf et al., 2018).

The angular unconformity separating the Oligocene volcanic rocks from the Eocene continental strata suggests a late Eocene compressional episode (Parada, 2008; Mosolf et al., 2018). On the other hand, the Oligocene to early Miocene rocks are affected by folds and thrusts, unconformably covered by the Quaternary volcanic rocks.

3. Methodology

Our methodology consists of: (i) structural mapping, (ii) 3D structural model construction, (iii) interpretation of Miocene and Quaternary stress fields from kinematic data of minor faults, (iv) slip and dilation tendency analysis for the main structures, (v) study of Coulomb stress variations after the 2004 earthquake event, and (vi) construction of a geomechanical model.

The field surveys were performed in the geothermal area, revealing the recent deformation, and along the Tinguiririca valley, providing a record of previous deformational events. The geology and stratigraphy rely mainly on previous cartography (Arcos, 1987; Arcos et al., 1988; Zapatta, 1995; Charrier et al., 1996; Parada, 2008; Aguirre et al., 2009; Clavero et al., 2011). As a base map, we used the

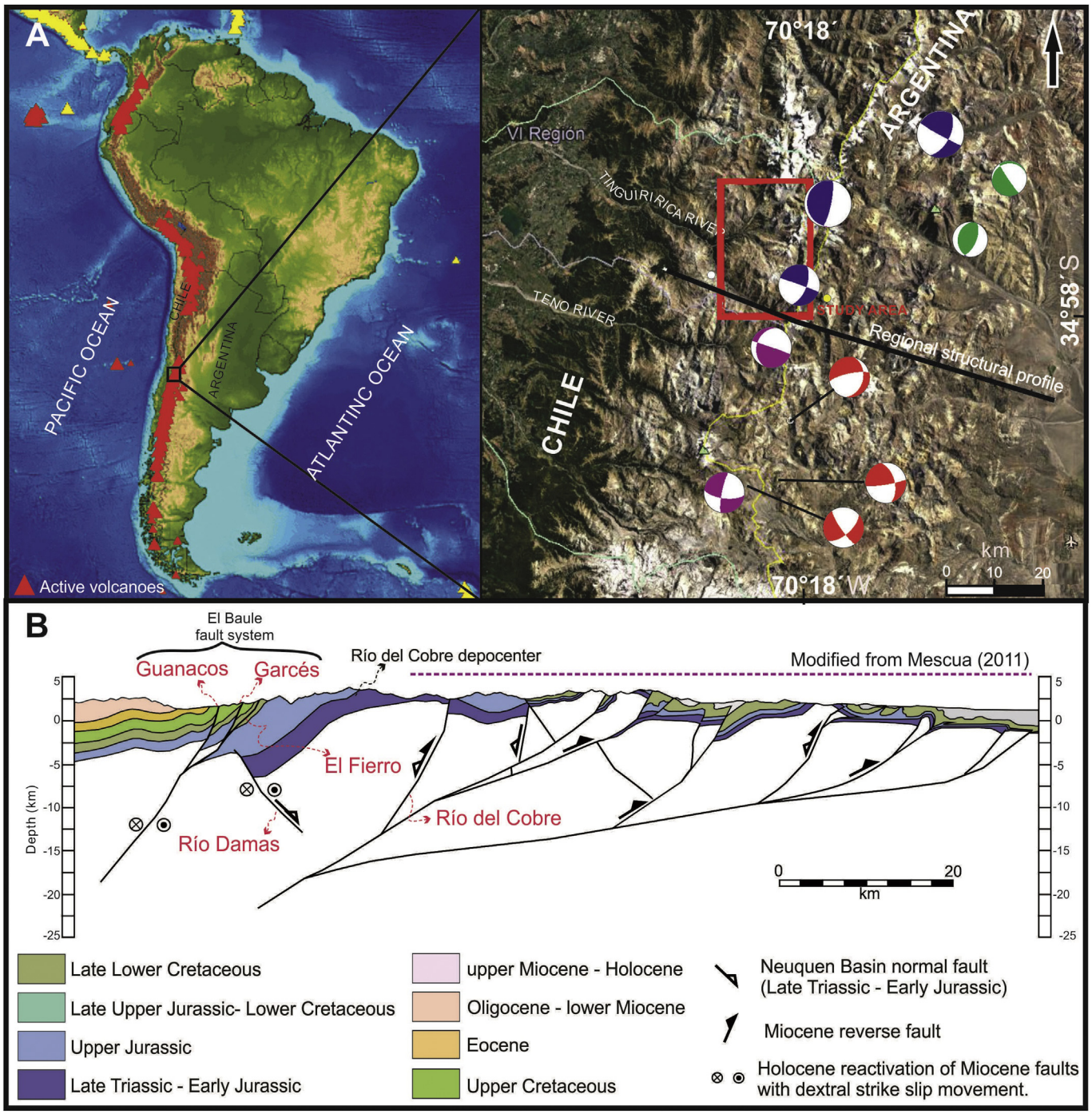

Figure 1. (A) Localization map in the Principal Cordillera of Chile with active volcanoes (red triangles), with the trace of the regional cross-section. Focal mechanisms (lower hemisphere compressional quadrants) are shown, obtained from CMT (Centroid Moment Tensor, Harvard, blue), Alvarado et al., (2005) (green), Spagnotto et al. (2015) (red), and Villegas et al. (2016) (violet). M_w 6.5 2004 earthquake is located within the study area. (B) Regional cross-section crossing the Andes at 35°S. The central and eastern sectors were modified from Mescua (2011).

latter (Clavero et al., 2011), which compiles all the available mapping and provides valuable new data. This geological map was updated and modified, based on the absolute ages provided by Mosolf et al. (2018) and our own data. During field work, we focused on the characterization of the main faults, their kinematics and timing of deformation. The kinematic analysis consists of obtaining the principal strain axes for the mapped structures, at scale 1:25,000, and the timing of deformation. We measured different types of kinematic indicators, such as crystal fibres on slip planes, iron-coated slickensides, and associated Riedel fractures, and then calculated the principal axes of shortening (λ_3) and extension (λ_1) for each incremental strain tensor associated with each fault-slip data, using the moment tensor summation method (Allmendinger, 2001).

In addition, we integrate the results of previous aeromagnetic, gravity and MT/TDEM (magnetotelluric/time domain electromagnetic) surveys conducted in the area (Clavero et al., 2011; Lira, 2011; Pavez et al., 2016), that show the presence of a major conductivity

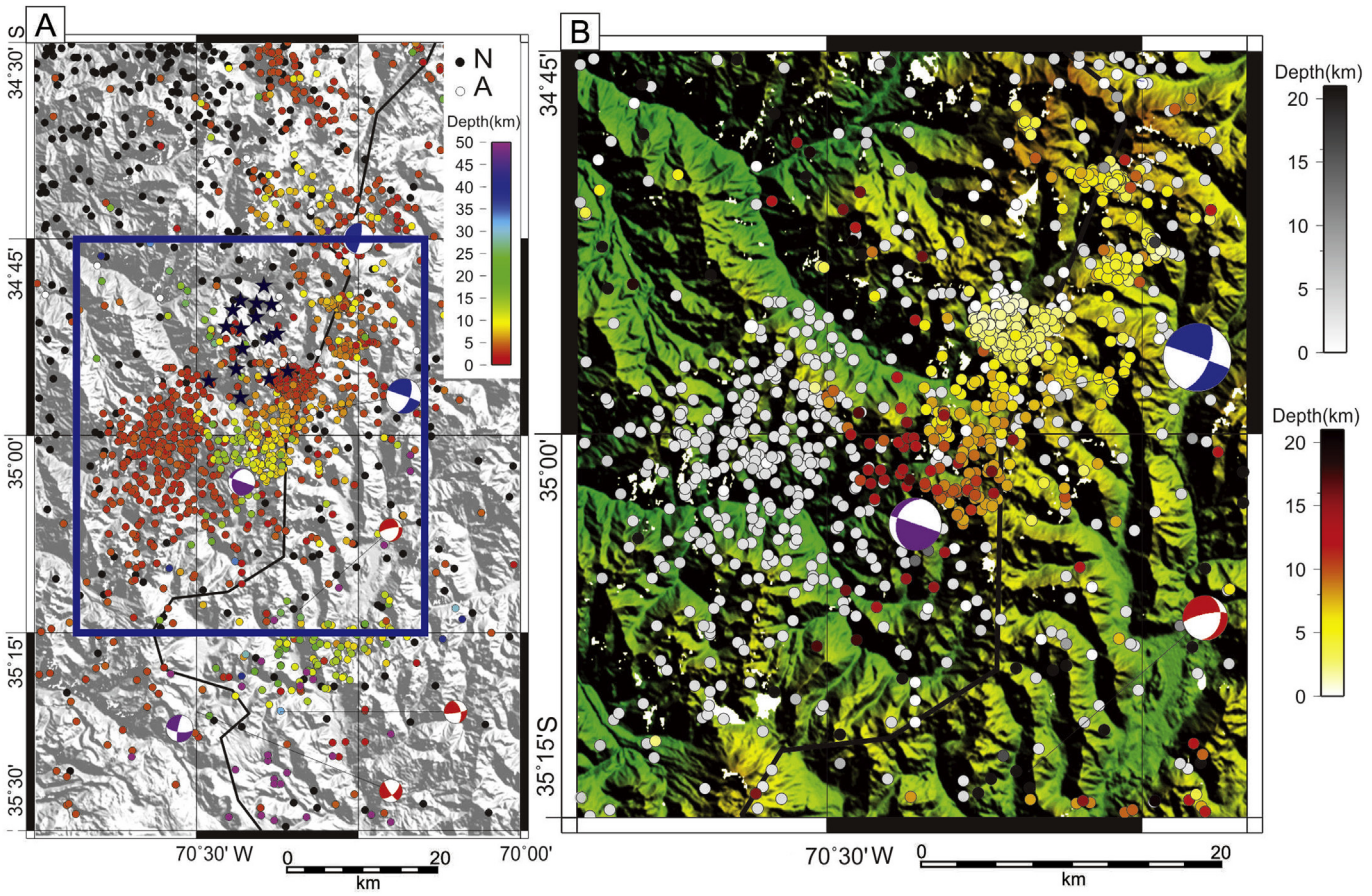

Figure 2. Seismicity maps. Epicenters from PDE catalog, Lira (2011) and Spagnotto et al. (2015) are shown with circles and focal mechanisms with beach balls (lower hemisphere compressional quadrants) from CMT catalog (blue), Spagnotto et al. (2015) (red) and Villegas et al. (2016) (magenta). Topography is taken from the Shuttle Radar Topography Mission. (A) Digital elevation model, showing the local network conducted by Lira (2011) (blue stars) and seismicity (circle colour-graded by depth). White dots represent earthquakes with epicenters above sea level, and black dots represent earthquakes at the subduction slab. (B) Detail map of seismicity registered in the study area, showing with live colours the depth of earthquakes registered during the 2010 local network (Lira, 2011), and with the grey scale the depths of other earthquakes.

anomaly on the southwestern flank of the Tinguiririca volcanic complex, and support the existence of a geothermal reservoir at depth (Clavero et al., 2011). Pavez et al. (2016) interpret the areas with a high Vp/Vs anomaly next to a low velocity area as being separated by a main fault, and regions with high Vp/Vs ratios to highly fractured damage zones. These authors interpret a decrease in the percentage variation of Vp (ΔVp), suggesting a decrease in the incompressibility elastic modulus, as the presence of hot fluid.

With detailed field data acquisition, we construct four ESE-striking balanced cross-sections with forward modelling, at a 1:25,000 scale. We used the 2D MOVE software to construct line-length and area-balanced cross-sections. Surface data were extrapolated to the pre-Cretaceous basement, using the flow-parallel fault algorithm and the interpretation of geophysical information as previously suggested by Pavez et al. (2016). Faults have been attributed in each section, and later merged into a 3D model, using MOVE2018.1 software. The 3D model dataset corresponds to the geological map, a digital elevation model (DEM), dip data, and the main fault surfaces. Fault surfaces created in the 3D model were meshed into regular triangles, using a tessellation algorithm from 3DMOVE.

The *in-situ* stress field is closely related to gravitational and tectonic stresses, and it can be described by the stress tensor, which includes the orientation and magnitudes of the three principal stresses (Engelder, 1993). The stress fields acting within the study area were inverted from fault-slip data sets obtained from meso-scale faults ($n = 284$). A best-fit reduced stress tensor was estimated for each structural station at a specific time, assuming the direction of slip on a plane, defined by the rake of the striae is parallel to that of the resolved shear stress (Wallace and Bott hypothesis). This method allows us to estimate the orientation of the principal stress axes (σ_1, σ_2, σ_3) and their relative magnitudes $\phi=(\sigma_2-\sigma_3)/(\sigma_1-\sigma_3)$ as defined by Angelier (1975), as well as the misfit angle (α) between the predicted and actual direction of slip. At each selected station, we measured meso-scale faults ($n \geq 10$), with as many different orientations as possible, and compared results obtained from different stations, located at variable distances from the principal faults. The age of fault activity was bracketed, considering the stratigraphic ages of affected and non-affected rocks. A fold-test was performed for each data taken from tilted beds. To obtain the paleostress tensor, we applied the Multiple-slip method implemented in the T-TECTO 3.0 program and used the Gauss method implemented by Zalohar and Vrabec (2007), to separate the heterogeneous data into homogeneous subsets. This method considers the compatibility between the direction of movement on the fault plane and the resolved shear stress (τ), and the ratio between the normal and shear stress (σ_n/τ) on the fault plane. The solutions agree with Amonton's Law, which states that a pre-existing fault plane is activated only when shear stress exceeds the frictional shear strength ($\tau > \mu_s \sigma'_n$). This allows the identification and separation of successive generations of faults and related stress regimes. The specific error (angle between measured

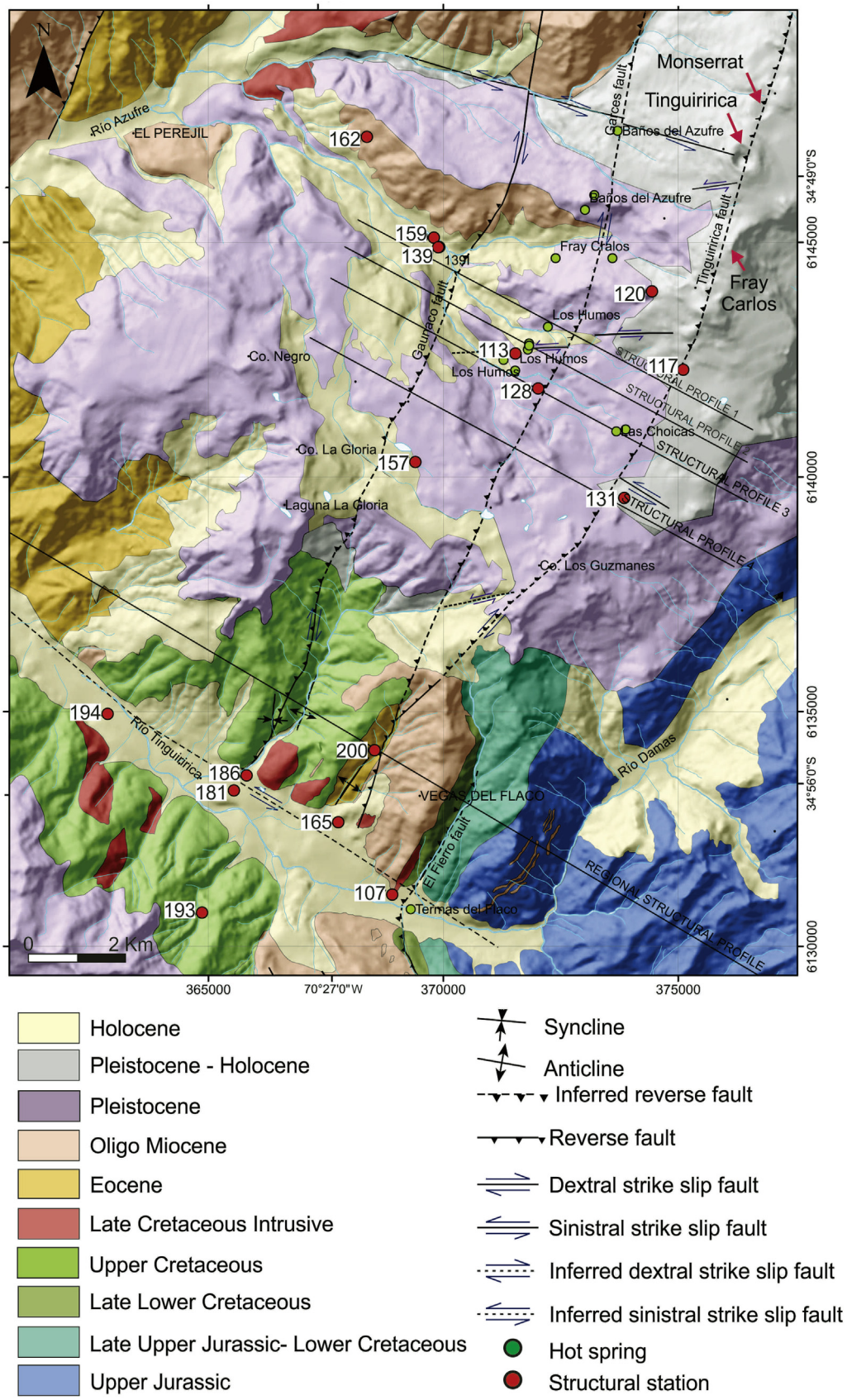

Figure 3. Geological map modified from Clavero et al. (2011) and Mosolf et al. (2018), showing the three main structures: the Guanacos, Garcés and Tinguiririca NNE-striking faults, the structural stations (red dots) and hot spring manifestations (green dots).

and theoretical slip orientation) for each datum does not exceed 25° for any of the studied faults.

We estimate the stress magnitudes at depth by considering both that the vertical stress at a certain depth is equal to the overburden pressure ($\sigma_v = \rho gz$), and that the frictional strength of faults and fractures (μ) distributed throughout the upper crust limits the maximum differential effective stress ($\sigma'_1 - \sigma'_3$) = [($\sigma_1 - P_f$)–($\sigma_3 - P_f$)] at depth (Jaeger and Cook, 1979; Zoback and Townend, 2001):

$$\sigma'_1/\sigma'_3 \leq [(\mu^2 + 1)^{1/2} + \mu]^2 \quad \text{(Eq. 1)}$$

Using Eq. 1 and values of frictional coefficient of 0.8, 0.6 and 0.4, in agreement with laboratory measurements (Byerlee, 1978; Jaeger and Cook, 1979) and inversion analysis (Reches, 1978; Martínez-Dias, 2002), we constrain σ'_1/σ'_3 to range between 4.32 and 2.16.

Considering the regular triangles of the fault surfaces and the orientation and shape of the stress tensors, we modelled the slip and dilation tendency (Morris et al., 1996; Moeck et al., 2009; Meixner et al., 2016) of the fault systems with the Stress Analysis module from MOVE. This analysis is used to determine the potential for reactivation of the main faults under the inferred stress field, and it provides clues about whether faults act as seals or conduits. Slip on a pre-existing fault occurs when the effective shear stress equals or exceeds the frictional resistance for sliding which is proportional to the effective normal stress resolved on the plane. Slip tendency is the ratio of effective shear stress to the effective normal stress on a surface and depends on the orientation of the fault segments with respect to the orientation of the principal stress axes and the $\phi = (\sigma_2 - \sigma_3)/(\sigma_1 - \sigma_3)$ value (Morris et al., 1996). Faults where shear stresses are high enough to overcome the frictional resistance are those well-oriented for reactivation. Higher slip tendency values for a given fault segment imply higher probability of slip. On the other hand, dilation tendency is the probability for a fault plane to open under the *in-situ* stress field (Ferrill et al., 1999).

With the assumption that the main faults are active structures, as indicated by field surveys, we used the Coulomb failure criterion ($\tau > \mu_s \sigma'_n$) to estimate under which mechanical conditions (friction coefficient μ, pore pressure P_f, cohesion C_o) faults reactivate. We initially set the C_o to 0. P_f was set to 0 and increased with 2 MPa intervals, until the main faults acquire a slip tendency >0.8. The same was done by setting the cohesion C_o to 10 MPa, to analyse the impact of hydrothermal precipitation along the fault plane, fault strengthening (Muhuri et al., 2003), over the dilation and slip tendencies and increasing P_f until a slip tendency >0.8. For every modelled fault we varied the frictional coefficient between 0.4 and 0.8. We assume target fault planes to be optimally oriented to slip (Table S1).

Earthquakes take place when the shear stresses are larger than the normal (or clamping) stresses that, in combination with friction, inhibit a locked fault from slipping (Freed, 2005). Slippage on a fault changes the stress field around it and may activate seismicity on adjacent faults (Stein, 1999; Freed, 2005). The stress changes on adjacent or receiver faults is calculated as the change in the Coulomb failure stress ($\Delta\sigma_F = \Delta\tau - \mu'\Delta\sigma_n$; Stein, 1999). Positive values indicate that the receiver faults have been brought closer to failure. We used a 3D elastic half-space boundary element model (Coulomb 3.2 software, Lin and Stein, 2004; Toda et al., 2005) to calculate how shear and normal stresses on neighboring faults are changed due to the M_w 6.5, 28/08/2004 earthquake with an epicenter in the study area (Fig. 2).

The Coulomb failure stress study requires knowledge of the regional stress field, the fault geometry, the slip distribution of the main shock, and the apparent friction coefficients. We test whether changes in stress after the 2004 nearby earthquake may affect the distribution of geothermal manifestations and we construct a kinematic-geomechanical theoretical model to explain the relationship between the main fault systems, and the creation of a plumbing system in the hydrothermal system.

4. Results

4.1. Structural mapping

The Mesozoic sedimentary strata and the lower Cenozoic volcanic and volcaniclastic rocks are folded and thrusted into a fault system known as El Baule (Mosolf et al., 2018), El Fierro (Farías et al., 2010; Tapia et al., 2015), Infiernillo-Los Cipreses (Piquer et al., 2010), or Maitenes-La Gloria (Parada, 2008); this fault system includes the Guanaco, Garcés and Tinguiririca faults. Overall, the contractional deformation affects rocks older than 11 Ma, as was pointed out by Mosolf et al. (2018). Quaternary volcanic rocks are subhorizontal and only affected by faults with strike-slip or normal kinematics.

The Guanaco and Garcés faults, previously recognized and mapped by Pineda (2010) and recently by Mosolf et al. (2018), are the main structures affecting the study area (Fig. 3). The **Guanaco fault** (Fig. 4A), also called El Baule fault (Zapatta, 1995; Parada, 2008; Muñoz et al., 2018; Mosolf et al., 2018), repeated and folded the Upper Cretaceous volcanic rocks. It is a >18 km long, NNE-striking and west dipping structure. Its core consists of a combination of clay-rich gouge, cataclasites and a complex fracture network, in a 100 m wide zone, surrounded by a damage zone with fractures and faults with a range of length and orientations (Fig. 4A). Strike separation of a dyke assigned to the Eocene (Mosolf et al., 2018) indicates 70 m of dextral horizontal displacement. Slickenlines in polished slip surfaces measured at station 1 and 2 (Fig. 4A) indicate that the fault has at least two movements. A reverse movement was measured at the western damage zone (station 1) and a dextral one with negligible oblique-slip components was measured in the core fault (station 2). The pre-tilted geometry of this structure corresponds to a reverse fault that has an angular relationship with the tilted strata between 30° and 40°. After tilting, the fault acquired its present high angle dip, between 65°W and 85°W. To obtain the kinematic axes for the contractional period, we back-tilted faults from station 1 restoring the strata to the horizontal position.

The **Garcés fault** (Figs. 4B and 5A) runs subparallel to the Guanaco fault, 2 km eastwards, for >15 km with a NNE strike. This fault places Upper Cretaceous volcaniclastic deposits over Eocene to Oligocene lavas, with a minimum net vertical displacement of 800 m. We measured meso-scale faults along the damage zones (sites 3 and 4 in Fig. 4B) showing both reverse and dextral strike-slip movements. In the present-day orientation, the fault appears as a subvertical structure, dipping between 60°W and 75°W, but the angular relationship between strata and fault plane varies between 25°S and 40°S. Close to the Los Humos geothermal manifestation, at point 128 (Fig. 3), a conjugate system E–W to ESE sinistral and NNE dextral meso-scale faults affecting the Pleistocene volcanic rocks were measured (Fig. 5A). At Baños de Azufre site, meso-scale faults present a N–S strike and pure dextral movement. Taken this data together, we interpret the Garces fault to control the localization of geothermal manifestations.

The **El Fierro fault**, named by Davidson (1971) in the Tinguiririca valley, can be observed in the southeastern sector of the study area. Although it is a well-recognized regional structure (Godoy and Palma, 1990; Godoy, 1991, 2015; Zapatta, 1995; Godoy et al., 1999; Charrier et al., 2002; Piquer et al., 2010), at the study latitude, it is a minor-displacement, low-angle reverse fault, verging eastward,

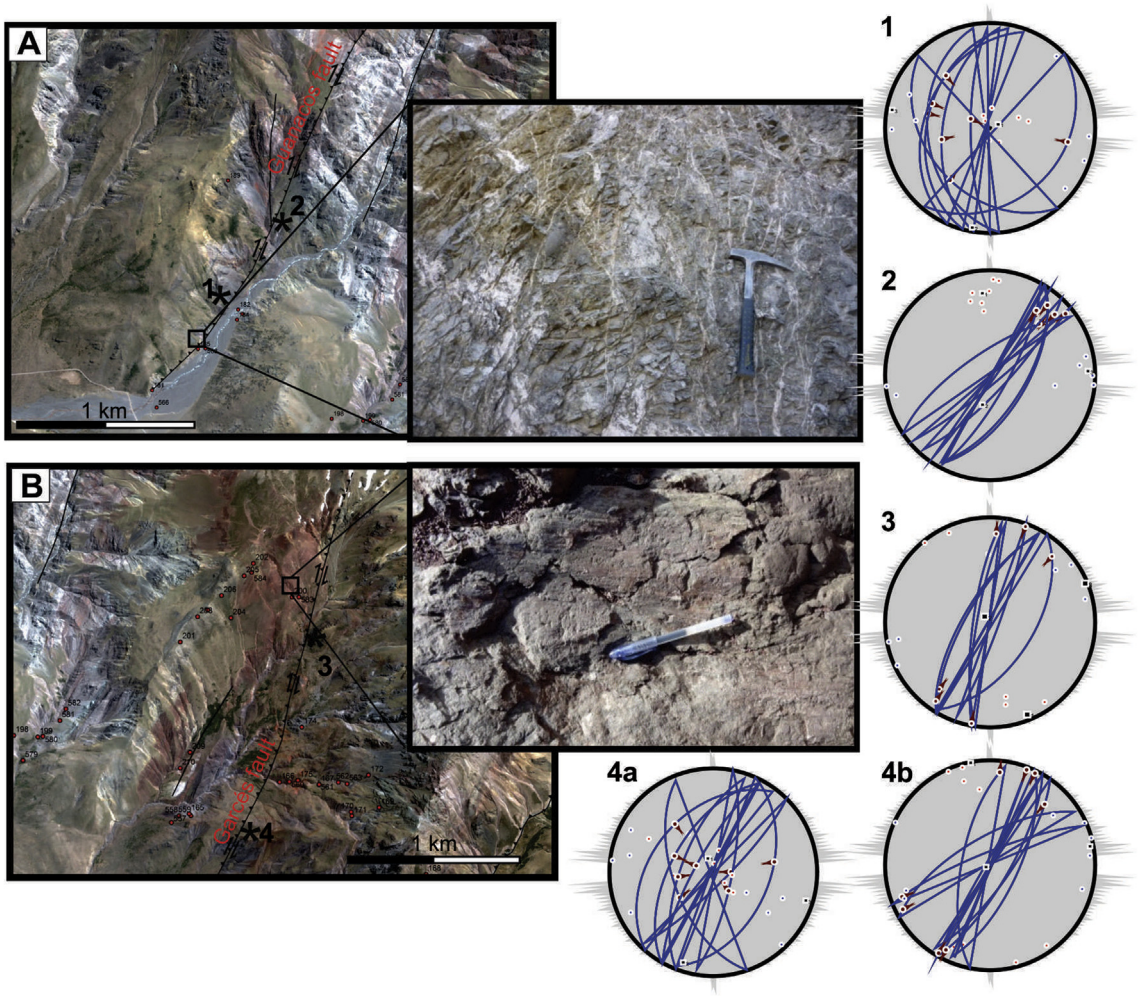

Figure 4. (A) Trace of the Guanaco fault close to the Tinguiririca valley, over a Google Earth image and outcrop photograph at station 181, showing a complex fracture network. Both reverse (1) and dextral (2) movements can be inferred from data. (B) Trace of the Garcés fault close to the Tinguiririca valley over a Google Earth image and detail photo of subhorizontal slickenlines. Stereonets showing faults (blue lines) and fault-slip data (red arrows indicating movement of hanging-wall with respect to the footwall), using FaultKinWin(R) program (Allmendinger, 2001). Both reverse (4a) and dextral (3 and 4b) movements can be inferred from data.

and affecting the Mesozoic and Paleogene sequences (Fig. 3) (Parada, 2008).

The **Tinguiririca fault** is marked as a NNE-trending volcanic lineament recognized in DEMs and satellite images (Fig. 3). This structure controls the orientation and emplacement of the Monserrat, Tinguiririca and Fray Carlos volcanoes. The fault is covered by Quaternary lavas, but at two sites (sites 117 and 131, Fig. 3) we measured meso-scale faults parallel to the main structure, suggesting it has a Quaternary activity. The kinematic of these faults indicate a pure dextral movement. At the Las Choicas area, there is clear association between the geothermal manifestations and NNE-dextral and E–W to ESE sinistral strike-slip meso-scale faults (Fig. 5B). Southwards, the trace of this structure merges into the Garcés fault trace, and it is interpreted here as a splay of that structure (Fig. 3).

The **Río Damas fault** is an interpreted structure, without surface expression (NNE-striking, ESE-dipping). This structure is associated with a low Vp/Vs anomaly (González, 2008, Fig. 6G,H) and seismicity registered in the area with a local network (Lira, 2011). Mescua et al. (2014) proposed that a normal fault with Upper Triassic–Lower Jurassic activity bounding the Neuquén basin half-graben on the western side was located near the interpreted Río Damas fault. Studies of the Lower Jurassic synrift deposits of the Nacientes del Teno Formation indicate an environment of proximal submarine fans with western provenance (Davidson, 1988), with paleogeographic reconstructions indicating emerged regions immediately to the west (Vicente, 2005). In the framework of the tectonics of the basin, this suggests that a normal fault controlled the western margin coinciding with the Río Damas fault. For the Upper Jurassic Río Damas Formation, also controlled by extensional tectonics in the area (Charrier et al., 2007; Mescua et al., 2008), thickness variations suggest that a master fault of a halfgraben also corresponds to the location of this structure (Mescua et al., 2014).

Second-order faults are observed in the Los Humos manifestation area (Fig. 3). These structures correspond to E–W to ESE sinistral faults, located between the Guanacos and Garcés faults, and between Garcés and Tinguiririca fault.

4.2. Three-dimensional structural model

We constructed four parallel balanced cross-sections separated by 2 km each, named 1 to 4 from north to south (the northern and southernmost are presented in Fig. 6) and extrapolated them into a 3D structural model (Fig. 7). The main structures are, from west to east, Guanacos, Garcés, Tinguiririca and Río Damas faults (Fig. 6A,B). The Garcés fault was the structure that achieved the biggest reverse displacement, modelled with 3.5 km of

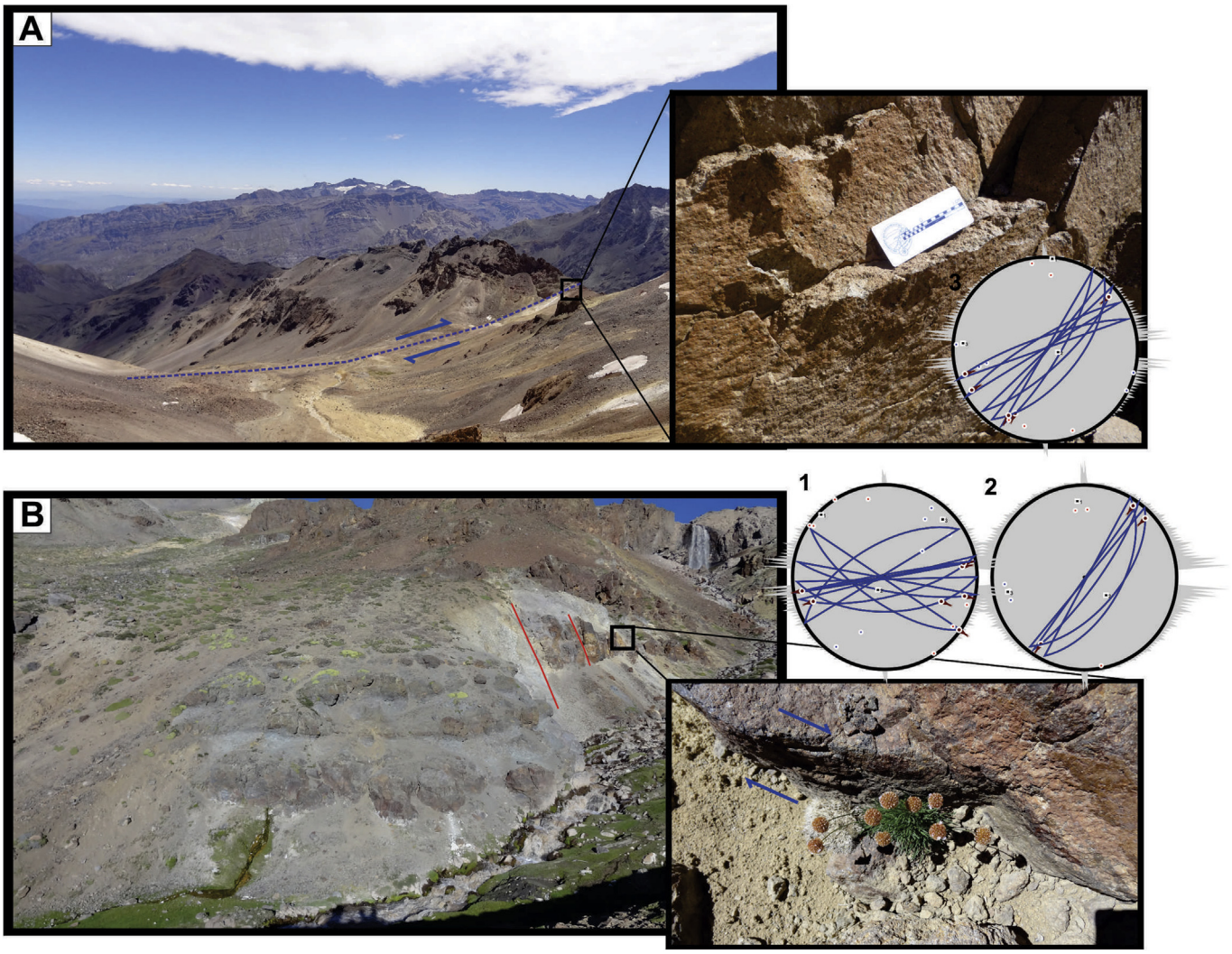

Figure 5. (A) The Garcés fault, close to the Los Humos geothermal area (34°51'30"S, 70°23'58"W), with outcrop photograph of subhorizontal dextral striaes. (B) Las Choicas geothermal manifestations close to the Tinguiririca fault area (34°52'30"S, 70°23'17"W), with outcrop photograph of fault plane and striaes, and kinematic data from meso-scale fault-slip data, showing ENE to ESE sinistral and NE dextral faults. See locations in Fig. 3.

displacement along the section 4. The Guanacos and Tinguiririca were modelled with 1.2 km and 2.6 km of horizontal shortening respectively, along the same section. In our model, the Guanaco and Garcés faults correspond to the same reverse fault system that affects the pre-Jurassic basement rocks and the Meso–Cenozoic sequences with an eastward vergence. The angular unconformities between the Oligocene, Eocene and older strata suggest that this system was active since the Eocene (Mosolf et al., 2018). The Tinguiririca fault corresponds to a splay of this system and only affects the Meso–Cenozoic sequences. The Río Damas fault is interpreted as a Triassic–Jurassic normal fault, not reactivated during the contractional period.

The 3D magnetotelluric resistivity imaging conducted by Clavero et al. (2011) indicates a very distinctive conductive layer (resistivity <10 Ohm-m), interpreted as the clay cap (argyllic alteration) of the system and confirmed by the well PTe-1. According to Clavero et al. (2011) and Pavez et al. (2016), the base of this layer marks the top of the geothermal reservoir (Fig. 6C,D). We interpret that the clay cap is broken off by the Garcés fault in the southern sector (cross-section 4, Fig. 5B), but not in the north (cross-section 1, Fig. 6A).

According to Clavero et al. (2011) and Pavez et al. (2016), the gravity study and the Vp/Vs anomalies reveal a magmatic chamber located below the Garcés and Tinguiririca faults and located between 3 km and 6 km b.s.l which provides the heat source for the geothermal system.

Seismic tomography interpretation suggests the existence of two velocity anomalies with relative low values of Vp, Vs and Vp/Vs, one located immediately to the west of the Tinguiririca and Fray Carlos volcanoes, named here as Termas anomaly, and the other one, Río Damas anomaly, in the Río Damas area (González, 2008; Lira, 2011; Pavez et al., 2016). According to Lira (2011) and Pavez et al. (2016), these anomalies are also related to low values of Vp*Vs (porosity parameter), suggesting high secondary porosity, and are interpreted by these authors as paths of hot fluid ascent related with fluid discharges at the hydrothermal areas. These authors interpreted the Termas seismic velocity anomaly, with low Vp (Fig. 6E,F), Vp/Vs (Fig. 6G,H) and Vp*Vs values, to be constrained in the uppermost 3000 m below surface, suggesting the presence of a high-fractured, permeable, and steam condensation zone. We interpreted this zone as a result of fracturing associated with movement of the Garcés and Tinguiririca faults. In our model

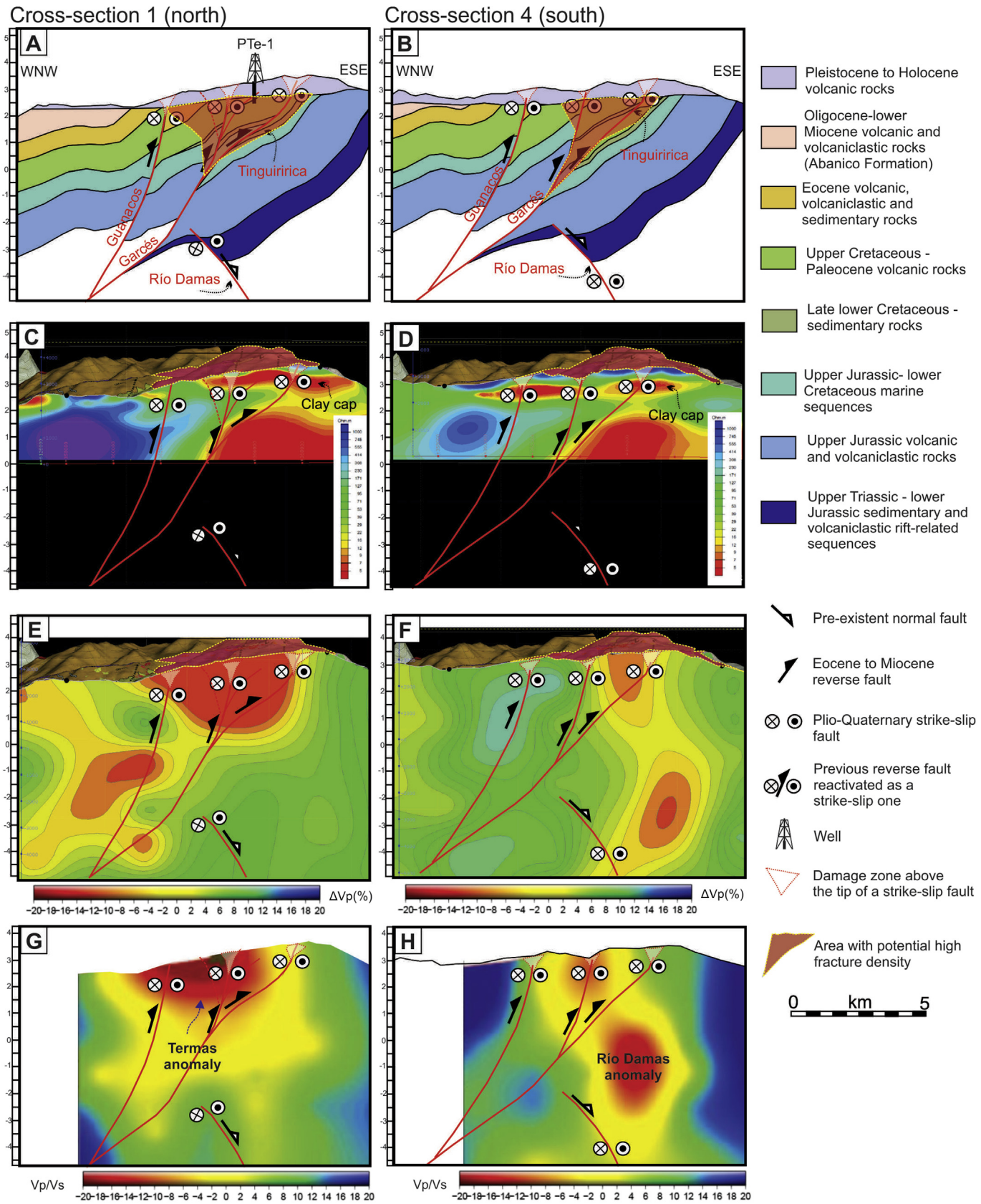

Figure 6. (A) Cross-section 1 (north). (B) Cross-section 4 (south). (C–D) Electrical resistivity sections for section 1 (C) and section 4 (D) from Clavero et al. (2011). (E–F) ΔVp from Lira (2011). (G–H) Vp/Vs values from Pavez et al. (2016).

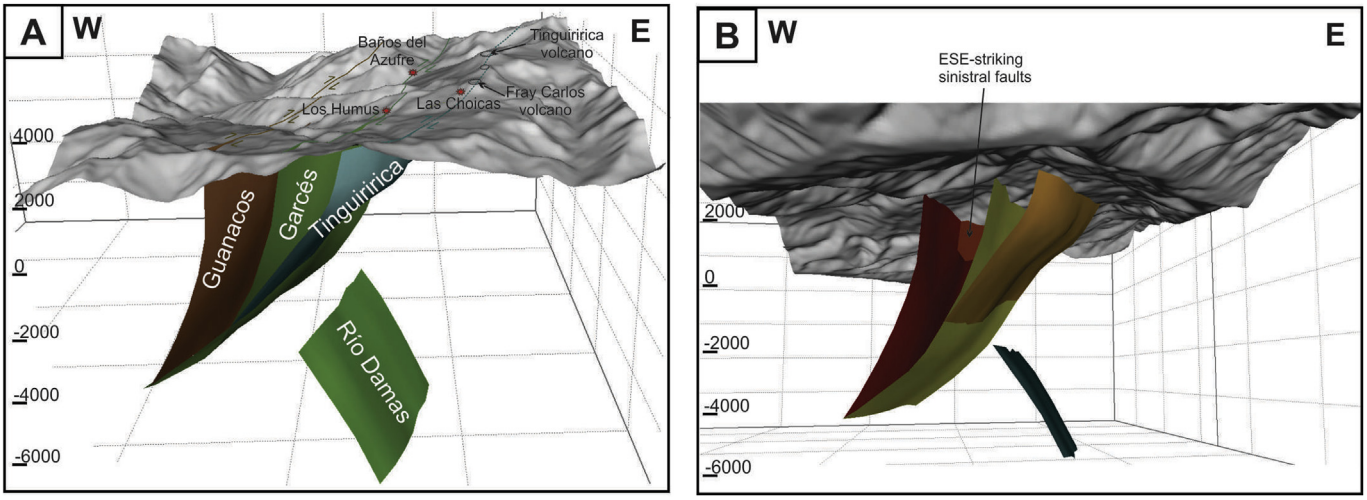

Figure 7. (A) 3D structural model, constructed by the extrapolation of fault line in each cross-section, showing the main faults affecting the Tinguiririca geothermal area. (B) 3D structural model, looking from below the surface.

(Fig. 7) the ESE-striking sinistral structures are responsible for the compartmentalization of the Termas seismic anomaly.

4.3. Stress and paleostress analysis

For the paleostress analysis, fault-slip data, including spatial orientation and associated striae of 284 meso-scale fault planes, with a centimeters-to-a-few-meters amount of movement, were collected from 17 sites across the study area (Fig. 3), and 17 stress tensor solutions were obtained (Table 1, Fig. 8 and S1). Fault-slip data were collected from: (i) tilted Upper Cretaceous to lower Miocene volcaniclastic rocks; and, (ii) subhorizontal Pleistocene to Holocene volcanic rocks. Except for site 120, all the calculated stress tensors show either compression or strike-slip stress regime (Fig. 8). The W–E compressional paleostress field has been identified at 5 sites, with SH_{max} average orientation of 105°, subperpendicular to the main fault strikes. This paleostress field is mostly detected at both sides of the Tinguiririca valley and in the Los Humos valley (Fig. 3) and it affects Upper Cretaceous to Miocene rocks older than 11.2 Ma, according to new ages from Mosolf et al. (2018), indicating that the last compressional event occurred prior to the late Miocene (>11 Ma).

Only in one site (139) was it necessary to separate the entire data into two consistent kinematic subsets, a compressional one (139a) and a strike-slip one (139b). The strike-slip faults affect all outcrops and correspond to a conjugate fault system with NNE dextral and E–W to ESE sinistral faults.

The strike-slip stress regime with ENE to ESE SH_{max} orientation (56° to 100°) is the most frequently observed and extends over most of the area. The mean tensor calculated for this stress field is $\sigma_1 = 77°$, $\sigma_3 = 167°$. The stress ratio varies between 0.4 and 0.6, suggesting a pure strike-slip stress regime, except for tensors 117 and 162, which show a strike-slip/normal regime, and tensor 193, which shows a strike-slip/reverse regime. The reactivation of the previously reverse Guanacos, Garcés and Tinguiririca faults as dextral strike-slip faults is explained by this regime.

Table 1
Table of data summarizing the results of the paleostress inversion. Parameters of the reduced stress tensors, with orientation (azimuth and plunge) of the principal stress axes ($\sigma_1 \geq \sigma_2 \geq \sigma_3$), ϕ ratio, and α misfit angle. nT: number of measured fault data, and n number of data used for each tensor determination. α: mean misfit angle. Stress regimes: C pure compression, C/SL compression/strike-slip, SL/C strike-slip/compression, SL pure strike-slip, SL/N strike-slip/extension, N/SL extension/strike slip. Q: accuracy parameter = n x (n/nt)/α (Delvaux et al., 1997). *Ar-Ar and +U-Pb ages from Mosolf et al. (2018).

Stress tensors												
Site	Latitude	Longitude	*n*	nT	σ_1	σ_2	σ_3	ϕ	α	Q	Regime	Age
107	34°57'21.03"S	70°26'49.79"W	10	10	285/2	15/002	150/87	0.5	17	B	C	< Cretaceous
113	34°50'59.92"S	70°24'18.52"W	11	14	86/13	292/76	177/6	0.53	15	B	SL	<Pliocene
117	34°51'12.83"S	70°21'58.12"W	10	10	100/8	265/68	007/17	0.8	23	C	SL/N	<Pleistocene
120	34°50'18.27"S	70°22'23.34"W	10	13	001/54	108/12	207/33	0.28	14	B	N/SL	<Pliocene
125	34°52'16.51"S	70°22'41.95"W	10	10	72/12	226/76	341/6	0.3	24	C	SL	<Pliocene
128	34°50'2.95"S	70°25'10.68"W	15	15	267/13	31/68	173/18	0.5	20	B	SL	<Pliocene
131	34°52'40.79"S	70°22'49.02"W	18	21	88/2	340/84	179/6	0.5	19	B	SL	<Pleistocene
139a	34°49'45.78"S	70°25'22.31"W	13	13	294/6	30/47	198/43	0.22	20	B	C/SL	<Oligo–Miocene
139b	34°49'45.78"S	70°25'22.31"W	55	55	236/2	344/84	145/6	0.49	24	A	SL	<Oligo–Miocene
157	34°52'14.10"S	70°25'43.47"W	10	10	260/2	009/84	170/6	0.5	15	B	SL	<Pliocene
159	34°49'39.01"S	70°25'25.28"W	10	10	253/13	99/76	345/6	0.7	8	B	SL	<Oligo–Miocene
162	34°48'28.49"S	70°26'20.25"W	22	24	67/23	262/66	159/6	1	25	B	SL/N	<Oligo–Miocene
165	34°56'23.65"S	70°26'51.20"W	16	17	100/13	193/12	325/73	0.6	20	B	C	<46.7 Ma*
181	34°55'59.07"S	70°28'19.66"W	22	22	101/2	010/12	200/78	0.4	19	B	C	<72.5 Ma*
186	34°58'29.27"S	70°33'9.95"W	9	9	062/2	160/72	333/18	0.52	22	C	SL	<72.5 Ma*
193	34°57'23.30"S	70°28'47.89"W	21	21	74/001	342/60	165/30	0.28	12	A	SL/C	<72.0 Ma*
194	34°55'6.77"S	70°30'4.81"W	11	11	239/13	116/68	333/18	0.5	18	B	SL	<74.0+ Ma
200	34°55'33.23"S	70°26'21.03"W	11	11	100/13	224/68	006/18	0.6	14	B	SL	<46.7 Ma*
total			284	296								

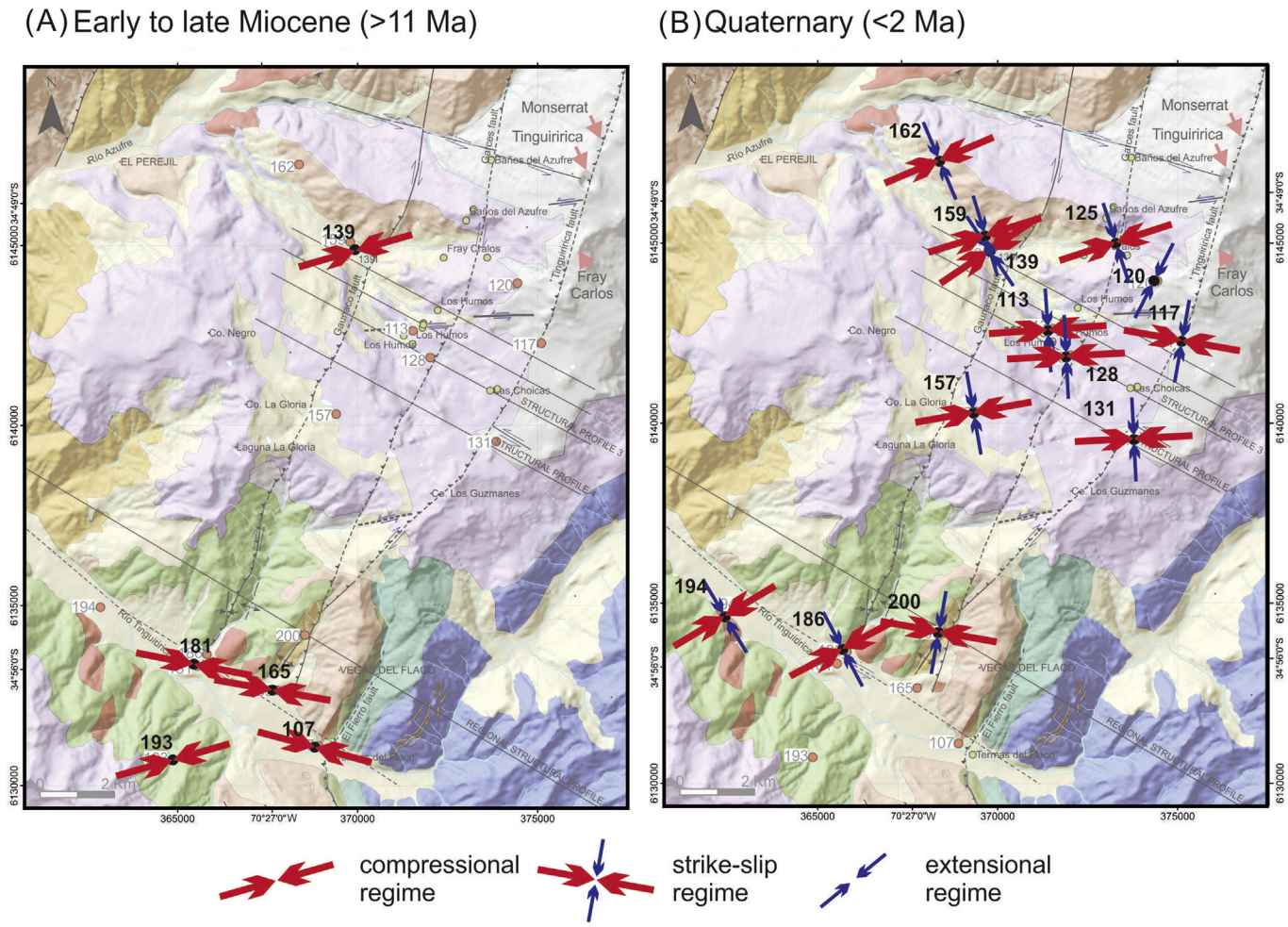

Figure 8. Paleostress maps for the pre-11 Ma period (A) and post-2 Ma period (B), showing the compressional and the strike-slip regimes that affected the area for the >11 Ma and <2 Ma periods, respectively.

Stress fields inferred from our fault-slip data, collected close to the main faults or inside the area between them, represent local stress fields which may be rotated with respect to the regional stress field (Twiss and Unruh, 1998). For this reason, we infer that the stress tensors calculated for sites outside these areas, such as sites 162, 193 and 194 (Fig. 3), represent a more regional stress field with ENE oriented σ_1 (66°) and NNE oriented σ_3 (156°), in agreement with focal mechanisms reported in the region (Fig. 2).

4.4. Slip and dilation tendency analysis

We estimate the magnitude of stress around the major faults with the aforementioned method and assumptions (Table S1), and conduct slip and dilation tendency analysis over the previously modelled major faults, to study the potential for tensile and shear failure along these structures associated with water or magma injection in the geological system under the Quaternary stress field.

Assuming that the intermediate stress axis (σ_2) is vertical, as appropriate for the analysed strike-slip regime, the vertical stress is calculated from the weight of the overburden rock. The reservoir is at ~2 km deep with an average rock density of 2.6 g/cm^3, giving a σ_v = 51 MPa. According to the frictional equilibrium (Eq. (1)) and the value of ϕ, we estimate that σ_1 ranges between 77 MPa and 154 MPa and σ_3 between 25 MPa and 49 MPa, assuming $\mu = 0.6$. For the deeply buried Río Damas fault, we estimate the σ_v = 102, at 4 km deep, and a medium value for ϕ (0.5). We also calculate the slip tendency with low (0.4) and high (0.8) friction coefficients to evaluate the effect of μ over the slip tendency of each target fault (Table S1).

The slip and dilation tendencies are calculated for the orientation and magnitude of the input stress tensors, in agreement with the observed end-members of the SHmax direction and the ϕ value range. For every fault, minimum and maximum slip tendency values are calculated corresponding to these end-members. The orientation of σ_1 for the Guanacos, Garcés and Tinguiririca faults are interpreted from the calculated reduced stress tensors at sites 159, 128 and 131, respectively (Fig. 3). We set cohesion to 0, which is a realistic assumption for pre-existing faults (Brace and Kohlstedt, 1980; Twiss and Moores, 1992), and to 10 MPa, in order to evaluate the effect of hydrothermal mineral precipitation.

Fluid pressure values required for failure vary according to the friction coefficient of each fault. The calculated fluid pressure required for failure with $\mu = 0.6$ ranges between 10 MPa and 15 MPa for the NNE-striking dextral faults, and between 0 and 10 MPa for the E–W to ESE striking sinistral faults. With a decrease in the friction coefficient ($\mu = 0.4$), the Garcés, Tinguiririca and Río Damas faults are prone to slip with less amount of fluid pressure (P_f = 10 MPa, Table S1). With a C_o set to 10 MPa, instead of 0, 3 MPa of extra fluid pressure is required to be established for the faults prone to slip (Table S1). The resulting slip tendency plots show that,

with $C_o = 0$, the Guanacos, Garcés and Tinguiririca faults have high slip tendency values (between 0.8 and 1) in their upper part, if the pore pressure is > 10 MPa for the Guanacos and Tinguiririca faults, or >15 MPa for the Garcés and Río Damas faults. There is a close direct relation between fault dip and the slip/dilation tendency, with high values of slip tendency distributed on the upper and steeper parts of the faults (Fig. 9). The steepest parts of the faults are the segments close to a critical stress state, whereas the rest of the structures require additional pore pressure values to induce slip (Fig. 9A).

The dilation tendency analysis shows that only the E–W to ESE subvertical, sinistral faults and, in a lesser extent, the Tinguiririca fault have high dilation tendency under the calculated in-situ stress field (Fig. 9B).

4.5. A case of Coulomb stress variations favouring fluid migration during the recent seismic cycle in a nearby source fault

Static stress changes caused by large earthquakes may result in permanent changes in hydrological processes, with the creation of new pathways and permeability enhancement. Manga et al. (2012) observed that small (<1 MPa) stresses, too small to produce new cracks or pathways, change fluid flow and fluid pressure. On the other handMoreover, changing permeability may result in local pore pressure changes (Brodsky et al., 2003), and may bring stable faults closer to failure as the effective normal stress locking the fault decreases.

For the 2004 M_w 6.5 mainshock event, with $M_0 = 7.16 \times 10^{16}$ Nm and strike-slip movement, Comte et al. (2008) and González (2008) reported M_w 6.7, at 34.93°S, 70.56°W and 4.7 km deep, and associated this earthquake to the El Fierro fault. ISC bulletin (http://www.isc.ac.uk/) reported at 34.98°S, 70.32°W and 6.5 km deep, with a minimum error of ±4.5 km in depth. González (2008) relocalized the aftershocks and proposed that this structure reaches 11 km deep. The focal mechanism (CMT) indicates the following planes: 21/61/-178 and 290/88/-29, and NEIC-PDE 24/69/-160 and 287/71/-23 https://earthquake.usgs.gov/earthquakes/eventpage/usp000d30e#moment-tensor. For this event, we calculate a subsurface rupture length of 28.6 km and width of 11 km, using the empirical relation defined by Wells and Coppersmith (1994), and slightly less (22.8 km and 12 km, respectively) using that by Leonard (2010). Considering the focal mechanisms reported by CMT and NEIC catalogs, we

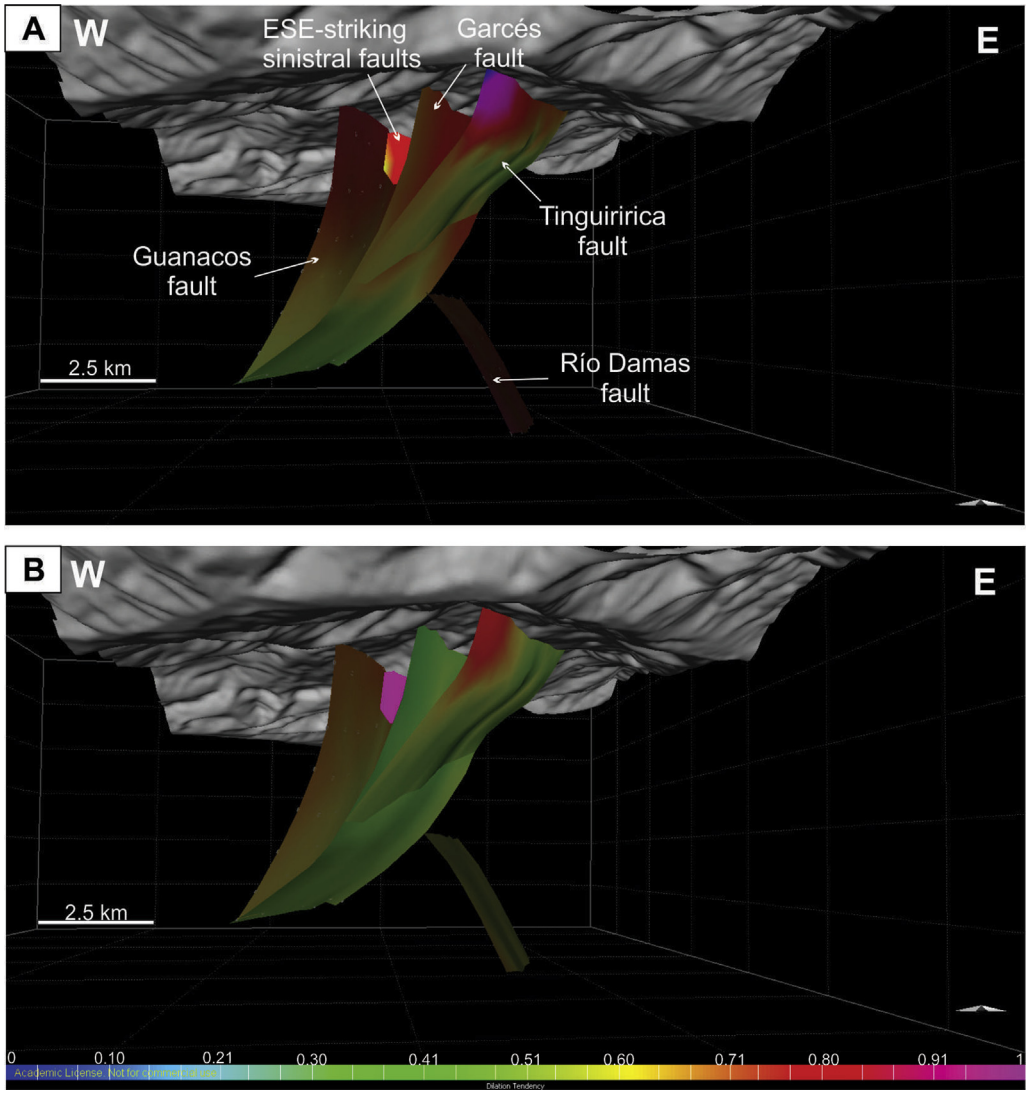

Figure 9. Slip tendency (A) and dilation tendency (B) analysis for the main structures: Guanacos, Garcés, Tinguiririca and Río Damas, and secondary ESE-striking sinistral faults. Results for values of fluid pressure of 15 MPa and μ = 0.6. The chromatic scale for both analyses is at the bottom of Fig. 9B.

suggest that fault motion associated with this event is the result of slip on the Río Damas fault (note the high slip tendency of this fault in the current stress regime, Fig. 9A). The location of the epicenter for this event was estimated from the aftershocks reported by Comte et al. (2008) and Lira (2011), and by the maximum intensities reported by USGS-NEIC (https://earthquake.usgs.gov/earthquakes/eventpage/usp000d30e # executive).

In our BEM (Boundary Element Model), we use the fault orientations and geometries presented in the 3D model, and evaluate the effect of static stress change on the likelihood of failure on the Guanacos, Garcés and Tinguiririca faults, considering them as target faults activated together with the Rio Damas fault. The calculated Coulomb stress change ($\Delta\sigma_F$) shows increased stress, up to 0.2 MPa in the upper tip of the Río Damas fault, in the sector where Lira (2011) registered seismicity during three months in 2010, confirming that positive static stress changes correlate with seismicity swarms (King et al., 1994; Hardebeck et al., 1998).

Furthermore, the 2004 M_w 6.5 earthquake produced positive changes of $\Delta\sigma_F$ values, which may bring the NNE-striking dextral Garcés and Tinguiririca faults closer to failure, potentially triggering them. Our calculation shows that the domains hosting geothermal manifestations correspond to domains of positive $\Delta\sigma_F$, suggesting that static stress changes exert a first-order control over permeability, increasing fluid circulation.

In addition, Lira (2011) reported earthquakes on the same structure (Río Damas fault) after the M_w 8.8, 27/02/2010 trench megafault, Maule earthquake, which suggests that crustal slip continues (Fig. 10).

5. Discussion: towards an integrated geomechanical model

Discriminating two of the main geothermal components, the recharge area and the reservoir, is key to understand a geothermal field. In a seismically active area, effective fluid focussing is critically reliant on active deformation to enhance permeability (Micklethwaite et al., 2010). In these areas, there are two different types of conduits. One conduit corresponds to the planes of active faults and the associated damage zones, where permeability is enhanced by dilation associated with slip on the planes (Barton et al., 1995; Cox, 1995; Aydin, 2000). The other type of conduit corresponds to high-permeability channels created by fracture-fault mesh systems at tips, fault intersections or step-overs (Curewitz and Karson, 1997; Marten and Boger, 1998; Sibson and Rowland, 2003). Curewitz and Karson (1997) have suggested that stress concentrations at these locations cause fracturing and reopening of fluid conduits. For this reason, identifying which fault or fault-fracture system is the most dominant factor in fluid flow is essential when characterizing the Tinguiririca field.

Kinematic data collected by Mosolf et al. (2018) indicate strike-slip and reverse movements of major faults. These authors proposed a transpressional shortening in the region from the late Eocene to late Miocene. On the other hand, Pavez et al. (2016) suggest that the main structures are reverse faults. Our data suggest two episodes of deformation separated in time, a first compressional event, with the development of the Guanaco and Garcés faults as reverse, east-vergent, low-angle structures, as suggested by Pavez et al. (2016) and Mosolf et al. (2018); followed by a strike-slip event, with the reactivation of these structure as dextral strike-slip faults. Rocks younger than 2 Ma are affected by NNE to N–S striking dextral faults, and E–W to ESE striking sinistral faults.

Our 3D structural model agrees with the model from Pavez et al. (2016), in that there is an important NNE-striking structure controlling the hydrothermal system, but differs from it in recognising the structure responsible for this. Pavez et al. (2016) interpreted the El Fierro reverse fault as the main structure governing the up-flow of hot fluids. In our model, the El Fierro fault is (north of El Fierro pass) a minor non-active reverse fault, whose tip point is located immediately to the north of the Tinguiririca River. On the contrary, we interpret that the main structures of the hydrothermal system are: (i) a deeply-seated fault system, characterized by Mosolf et al. (2018) as the El Baule fault system; and (ii) the Río Damas blind fault. We propose that the 2004 M_w 6.5 earthquake occurred on the Río Damas highly dipping dextral fault. This event was associated with a cluster of earthquakes, registered during the 2010 survey (Lira, 2011), located in an area that experienced maximum static stress change after the main 2004 event. Fig. 10 shows that the 2010 seismic swarm formed a cluster around the tip segment of the Rio Damas activated segment. Our analysis shows that both the reactivation of faults, determined by the *in-situ* stress field, and the permeability enhancements in the shallow crust, due to the proximity to an active major fault buried at depth, localize hydrothermal manifestation at the surface. A strong directional permeability, parallel to σ_2, may promote the migration of fluids through a mesh of shear and extension fractures, parallel to the fault-fracture intersections (Hill, 1977; Sibson, 1996). In the strike-slip regime that governs deformation since the late Miocene (<11 Ma), this direction is vertical, and has favoured upward fluid circulation from above the magma chamber into the uppermost shallower crustal levels.

Our investigations indicate that the permeability in the Tinguiririca geothermal field is dominated by two different mechanisms: (i) conduits created by shear along active shallow crustal strike-slip faults; and, (ii) failure along a fracture-fault mesh connecting both major structures as a result of positive Coulomb stress change. The small stress changes suggest that faults are close to failure, which may be related to an elevated pore fluid pressure (Hill et al., 1993). The distribution of the 2010 seismicity registered by Lira (2011) is likely to be related to a release of a pulse of overpressured fluids from a fluid reservoir (Koerner et al., 2004; Miller et al., 2004).

The three main faults, Guanacos, Garcés and Tinguiririca, are nearly optimally oriented in the present-day stress field, and all of them present evidence of either Pleistocene or Holocene dextral strike-slip movement. The slip and dilation analyses suggest that conduits created by shearing within the main three faults may be responsible for hot fluid migration, but additional factors, such as high fluid pressure, may promote failure and increase in permeability. We suggest that the higher permeability along the Tinguiririca and Garcés faults is related to their locations above the Río Damas fault, and close to the area of seismic swarm registered during the 2010 survey (Lira, 2011), interpreted here as an active fracture-fault mesh (Fig. 11). In this scenario, we predict geothermal manifestations to coincide with the region of positive Coulomb stress change, close to the main conductive structure. We propose that higher permeability in the Garcés and Tinguiririca faults may be driven by high-pressure fluids propagating through this fracture network. The very high dilation tendency of the W–E to ESE sinistral faults, constrained between both the Guanacos and Garcés, and between Garcés and Tinguiririca faults, may control fluid migration between these conduit systems. This is supported by the interruption of the highly conductive layer at the Garces fault sector (Fig. 6C), which is thought to have split the conductive horizon into two and also to have set an eastern limit on its northern half. This implies recent fault activity, supported by the fact that the main hot springs are aligned along the trace of this fault (Fig. 3).

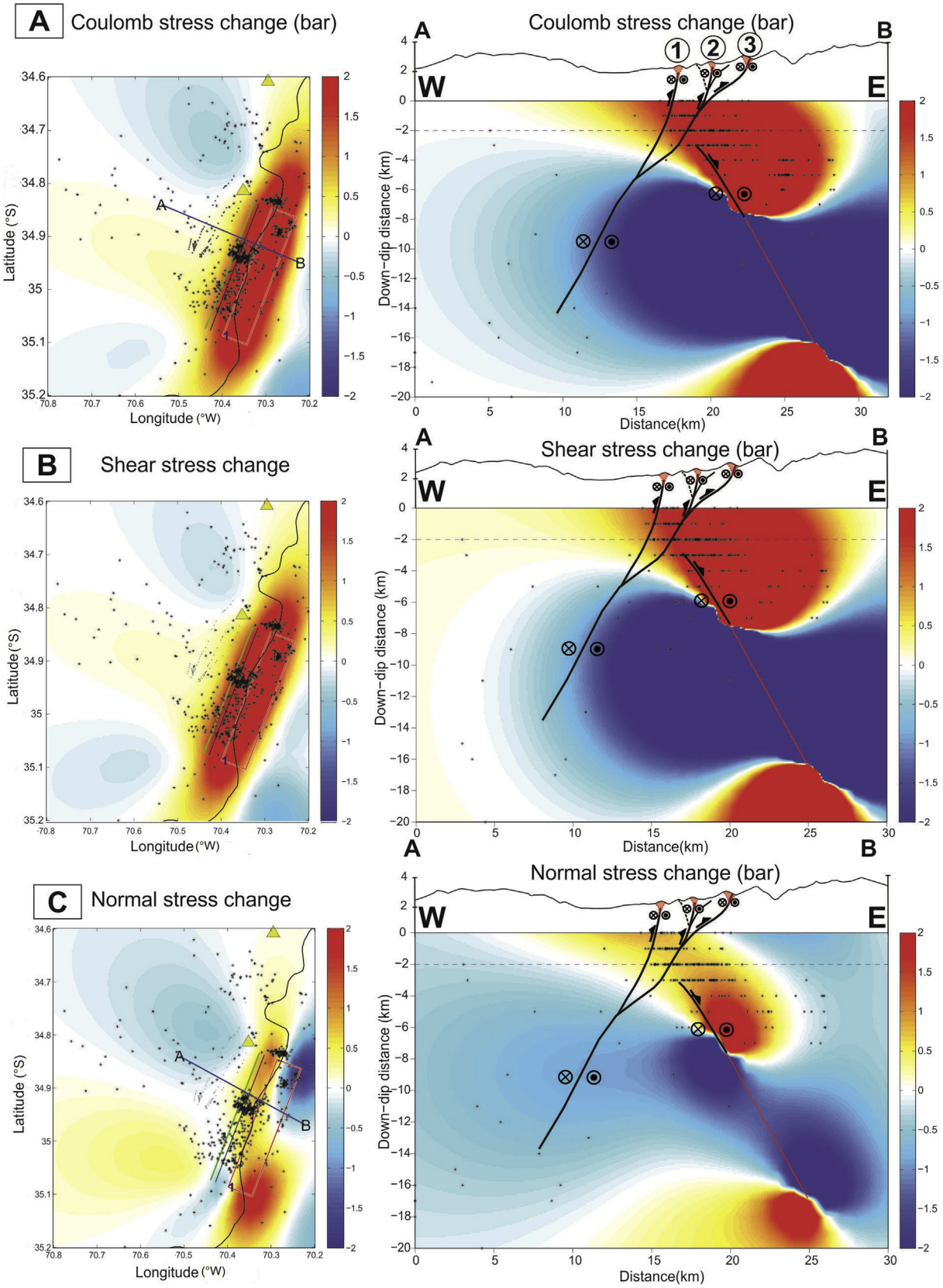

Figure 10. Map and cross-section of Coulomb static stress change in receptor fault planes, with strike 25°, dip 60°E, and rake 180° (pure dextral movement) at depth of 2 km, with cross sections A–B. Numbers 1, 2 and 3 representing the Guanacos, Garcés and Tinguiririca faults, respectively. Source: Earthquake M_w 6.5, 2004. (A) Total stress change, (B) shear static stress change, and (C) normal stress change. Black points: earthquakes that occurred in 2010, modified from Lira (2011).

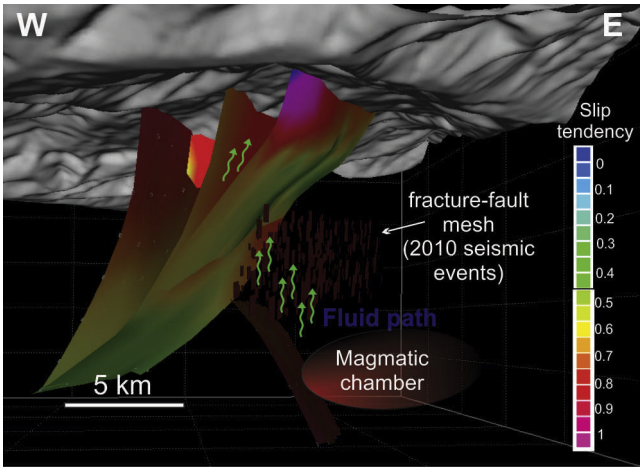

Figure 11. Conceptual geomechanical model proposed for the Tinguiririca geothermal field. The upper part of the three main faults, Guanacos, Garcés and Tinguiririca, are nearly optimally oriented in the present-day stress field. The inferred Río Damas fault has high slip tendency (>0.8), and a strike-slip movement along it is interpreted as the source of the 2004 M_w 6.5 earthquake event. Our model proposes that the permeability in the Tinguiririca geothermal field is dominated by two different mechanisms: conduits created by shear along active shallow crustal faults, mainly Río Damas, Garcés and Tinguiririca; and, failure along a fracture-fault mesh connecting both major structures as a result of positive Coulomb stress change.

6. Conclusions

By means of a multidisciplinary approach, we explore the spatial relationship between faults, active hot springs and local seismicity, and demonstrate their close association. For this purpose, we investigate the fault stress state, local seismic activity, and fluid circulation in the Tinguiririca geothermal system, in the southern Central Andes (35°S). This geothermal system is affected by: (i) three NNE-striking faults, the Guanacos, Garcés and Tinguiririca faults; (ii) an inferred deeply seated Río Damas fault; and (iii) second-order subvertical W–E to ESE striking faults constrained between the main structures. The paleostress analysis, with inversion modelling of 284 fault-slip data collected from 17 sites across the study area, determined for the arc region, evidences two main tectonic events, a compressional one that occurred previous to late Miocene (>11 Ma) and a Quaternary strike-slip one affecting all the outcropping rocks (<2 Ma). Our study suggests that the main faults in the area, Guanacos and Garcés, are not new faults, but previous reverse faults, subsequently tilted and reactivated as strike-slip faults.

With the paleostress analysis, we conduct slip and dilation tendency analysis over the previously-modelled faults, and we quantify the likelihood of failure along these structures in terms of their state of stress. The results show that the main structures have high slip tendency and are close to failure, providing excellent pathways for hot fluids.

For the main active strike-slip faults, Guanacos, Garcés and Tinguiririca, we estimate Coulomb static stress changes produced by the 2004 M_w 6.5 mainshock event. The associated slip of this event is related to movement along the Río Damas fault. This earthquake produced positive changes of Coulomb static stress on the main structure planes, in the area where subsequent seismicity is registered during the 2010 survey. We interpret this area as a fracture-fault mesh at the tip of the Río Damas fault, where high permeability is responsible for the hydrothermal up-flow and is maintained by seismic activity.

Considering the 3D structural model, the inferred Quaternary stress field, the dilation and slip tendency of the different fault systems, and Coulomb stress variations after the 2004 earthquake located along the Río Damas fault, we construct a geomechanical model to explain the relationship between the main faults, *in-situ* stress field variations and the creation of a plumbing system in the hydrothermal field. Our geomechanical model proposes that the permeability in the Tinguiririca geothermal field is dominated by two different mechanisms: (i) conduits created by shear along active shallow crustal faults; and, (ii) failure along a fracture-fault mesh connecting major structures, the Garcés and Tinguiririca faults, as a result of positive Coulomb stress change.

Acknowledgements

This research was supported by a grant from the Agencia Nacional de Promoción Científica y Tecnológica (PICT 2011-1079) to Giambiagi. The authors want to thank Energía Andina S.A. for providing geological and geophysical information. We would like to acknowledge the T-TECTO 3.0 Professional and MOVE.2018 academic licenses to IANIGLA. This manuscript benefited from very helpful reviews by two anonymous reviewers, and by Guest Editors Silvia Japas, Sebastian Oriolo and Vinod Samuel who are acknowleged.

Appendix A. Supplementary data

Supplementary data to this article can be found online at https://doi.org/10.1016/j.gsf.2019.02.006.

References

Aguirre, L., Calderón, S., Vergara, M., Oliveros, V., Morata, D., Belmar, M., 2009. Edades isotópicas de rocas de los valles Volcán y Tinguiririca, Chile central. In: 12° Congreso Geológico Chileno, Santiago. S8_001.

Allmendinger, R.W., 2001. FaultKinWin Version 1.2.2. A Program for Analyzing Fault Slip Data for Windows Computers. http://www.geo.cornell.edu/geology/faculty/RWA/programs.html.

Alvarado, P., Beck, S., Zandt, G., Araujo, M., Triep, E., 2005. Crustal deformation in the south-central Andes backarc terranes as viewed from regional broad-band seismic waveform modelling. Geophysical Journal International 163 (2), 580–598.

Angelier, S., 1975. Sur l'analyse de mesures recueillies dans des sites faillés: l'utilité d'une confrontation entre les méthodes dynamiques et cinématiques. Comptes Rendus de l'Académie des Sciences 281, 1805–1808.

Arcos, J., 1987. Geología del Cuadrángulo Termas del Flaco, Provincia de Colchagua, VI Región, Chile. Memoria de Título, Departamento de Geología y Geofísica, Universidad de Chile, p. 279.

Arcos, J., Charrier, R., Munizaga, F., 1988. Volcanitas cuaternarias en la hoya superior del río Tinguiririca (34°40′LS- 70°21′LW): características geológicas antecedentes, geoquímicos y geocronológicos. In: 5° Congreso Geológico Chileno, Actas, 3, pp. 1245–1260.

Aydin, A., 2000. Fractures, faults, and hydrocarbon entrapment, migration and flow. Marine and Petroleum Geology 17, 797–814.

Barton, C.A., Zoback, M.D., Moos, D., 1995. Fluid flow along potentially active faults in crystalline rocks. Geology 23, 683–686.

Benavente, O., 2015. Origen y naturaleza de los fluidos en los sistemas volcánicos e hidrotermales activos de los Andes de Chile Central (32.5-36°S). Doctoral Thesis. Departamento de Geología, Universidad de Chile, p. 274 (in Spanish with English abstract).

Benavente, O., Aguilera, F., Gutiérrez, F., Tassi, F., Reich, M., Vaselli, O., 2012. Los sistemas hidrotermales de Chile Central (33-36°S). In: 13o Congreso Geológico Chileno, pp. 559–561 (in Spanish with English abstract).

Bonali, F.L., tibaldi, A., Corazzato, C., Tormey, D.R., Lara, L., 2013. Quantifying the effect of large earthquakes in promoting eruptions due to stress changes on magma pathway: the Chile case. Tectonophysics 583, 54–67.

Brace, W.F., Kohlstedt, D.L., 1980. Limits on lithospheric stress imposed by laboratory experiments. Journal of Geophysical Research Solid Earth 85 (B11), 6248–6252.

Brodsky, E., Roeloffs, E., Woodcock, D., Gall, I., Manga, M., 2003. A mechanism for sustained groundwater pressure changes induced by distant earthquakes. Journal of Geophysical Research 108 (B8), 2309. https://doi.org/10.1029/2002JB'002321.

Byerlee, J.D., 1978. Friction of rocks. Pure and Applied Geophysics 116, 615–629.

Cembrano, J., Lara, L., 2009. The link between volcanism and tectonics in the southern volcanic zone of Chilean Andes: a Review. Tectonophysics 471, 96–113.

Charrier, R., Wyss, A.R., Flynn, J.J., Swisher, C., Norell, M.A., Zapata, F., McKenna, M.C., Novacek, M.J., 1996. New evidence for late mesozoic-early cenozoic evolution of the Chilean Andes in the upper Tinguiririca Valley (35'S), Central Chile. Journal of South American Earth Sciences 9, 393–422.
Charrier, R., Baeza, O., Elgueta, S., Flynn, J.J., Gans, P., Kay, S.M., Muñoz, N., Wyss, A.R., Zurita, E., 2002. Evidence for Cenozoic extensional basin development and tectonic inversion south of the flat-slab segment, southern Central Andes, Chile (33o-36oS). Journal of South American Earth Sciences 15, 117–139.
Charrier, R., Pinto, L., Rodríguez, M.P., 2007. Tectono-stratigraphic evolution. In: Moreno, T., Gibbons, W. (Eds.), The Geology of Chile. The Geological Society, London, pp. 21–114.
Clavero, J., Pineda, G., Mayorga, C., Giavelli, A., Aguirre, I., Simmons, S., Martini, S., Soffia, J., Arriaza, R., Polanco, E., Achurra, L., 2011. Geological, geochemical, geophysical and first drilling data from Tinguiririca Geothermal Area, Central Chile. GRC Transactions 35, 731–734.
Comte, D., Farías, M., Charrier, R., González, A., 2008. Active tectonics in the Central Chilean Andes: 3D tomography based on the aftershock sequence of the 28 August 2004 shallow crustal earthquake. In: 7o International Symposium on Andean Geodynamics (ISAG 2008, Nice), pp. 160–163.
Cox, S.F., 1995. Faulting processes at high fluid pressures: an example of fault-valve behaviour from the Wattle Gully Fault, Victoria, Australia. Journal of Geophysical Research 100 (12), 841-12,859.
Cox, S.F., 2005. Coupling between deformation, fluid pressures, and fluid flow in ore-producing hydrothermal systems at depth in the crust. Economic Geology 100th Anniversary Volume 39–75.
Curewitz, D., Karson, J.A., 1997. Structural settings of hydrothermal outflow: fracture permeability maintained by fault propagation and interaction. Journal of Volcanology and Geothermal Research 79, 149–168.
Davidson, J., 1971. Contribución al estudio geológico de los Andes Meridionales Centrales: Geología del área de las Nacientes del Teno, Provincia de Curicó. Thesis. Departamento de Geología, Universidad de Chile, Santiago, p. 145 (in Spanish).
Davidson, J., 1988. El Jurásico y Cretácico inferior en las nacientes del río Teno (Chile): una revisión. In: 5º Congreso Geológico Chileno, Actas, 1, pp. 453–458 (in Spanish).
Delvaux, D., Moeys, G., Stapel, C., Petit, K., Levi, A., Miroshnichenko, V., Ruzhich, A.D., Sankov, V., 1997. Paleostress reconstructions and geodynamics of the Baikal region, central Asia, Part 2. Cenozoic rifting. Tectonophysics 282, 1–38.
Druitt, T., Costa, F., Deloule, E., Dungan, M., Scaillet, B., 2012. Decadal to monthly timescales of magma transfer and reservoir growth at a caldera volcano. Nature 482, 77–80.
Engelder, T., 1993. Stress Regimes in the Lithosphere. Princeton University Press, Princeton, p. 457.
Farías, M., Vargas, G., Tassara, A., Carretier, S., Baize, S., Melnick, D., Bataille, K., 2010. Land-level changes produced by the Mw 8.8 2010 Chilean earthquake. Science 329 (5994), 916-916.
Faulkner, D.R., Jackson, C.A.L., Lunn, R.J., Schlische, R.W., Shipton, Z.K., Wibberley, C.A.J., Withjack, M.O., 2010. A review of recent developments concerning the structure, mechanics and fluid flow properties of fault zones. Journal of Structural Geology 32, 1557–1575.
Ferrill, D.A., Stamatakos, J.A., Sims, D., 1999. Normal fault corrugation: implications for growth and seismicity of active normal faults. Journal of Structural Geology 21 (8–9), 1027–1038.
Freed, A.M., 2005. Earthquake triggering by static, dynamic, and postseismic stress transfer. Annual Review of Earth and Planetary Sciences 33, 335–367.
Godoy, E., 1991. El Corrimiento del Fierro reemplaza a la discordancia intrasenoniana en el río Cachapoal, Chile Central. In: 10o Congreso Geológico Chileno, pp. 635–639.
Godoy, E., 2015. The north-western margin of the Neuquén Basin in the headwater region of the Maipo drainage, Chile. In: Sepúlveda, S.A., Giambiagi, L.B., Moreiras, S.M., Pinto, L., Tunik, M., Hoke, G.D., Farías, M. (Eds.), Geodynamic Processes in the Andes of Central Chile and Argentina, vol. 399. Geological Society, London, Special Publications. https://doi.org/10.1144/SP399.13.
Godoy, E., Palma, W., 1990. El Corrimiento del Fierro y su propagación en el alto río Maipo, Andes de Chile central: un evento Oligoceno a Mioceno inferior. In: 1o Simposio sobre el Terciario de Chile, pp. 97–104 (in Spanish).
Godoy, E., Yáñez, G., Vera, E., 1999. Inversion of an Oligocene volcano-tectonic basin and uplifting of its superimposed Miocene magmatic arc in the Chilean Central Andes: first seismic and gravity evidences. Tectonophysics 306, 217–236.
González, A.C., 2008. Análisis estructural entre los valles del río Tinguiririca y Teno, Cordillera Principal de Chile Central: Microsismicidad y geología superficial. Memoria Universidad de Chile, p. 90 (in Spanish with English abstract).
Hardebeck, J.L., Nazareth, J.J., Hauksson, E., 1998. The static stress change triggering model: constraints from two southern California aftershock sequences. Journal of Geophysical Research 103 (24), 427-24,437.
Hill, D.P., 1977. A model for earthquake swarms. Journal of Geophysical Research 82 (8), 1247–1352.
Hill, D.P., Reasenberg, A., Arabaz, W.J., Beroza, G., Brumbaugh, D., Brune, J.N., Castro, R., Davis, S., dePolo, D., Ellsworth, W.L., Gomberg, J., Harmsen, S., House, I., Jackson, M.J.S., Jones, L., Keller, R., Malone, S., Munguia, L., Nava, S., Pechmann, J., Sanford, C.A., Simpson, R.W., Smith, R.B., Stark, M., Stickney, M., Vidal, A., Walter, S., Wong, V., Zollweg, J., 1993. Seismicity remotely triggered by the magnitude 7.3 Landers, California, earthquake. Science 260, 1617–1623.
Hubbert, M., Rubey, W.W., 1959. Role of fluid pressure in mechanics of overthrust faulting: I. Mechanics of fluid-filled porous solids and its application to overthrust faulting. The Geological Society of America Bulletin 70 (2), 115–166.
Iannelli, S., Fennell, L., Litvak, V., Fernández, P., Encinas, A., Folguera, A., 2018. Geochemical and tectonic evolution of late cretaceous to early Paleocene magmatism along the southern central Andes (35-36°S). Journal of South American Earth Sciences 87, 139–156.
Jaeger, J.C., Cook, N.G., 1979. Fundamentals of Rock Mechanics, third ed. Chapman and Hall, New York, Chapman and Hall, p. 593.
King, G.C.P., Stein, R.S., Lin, J., 1994. Static stress changes and the triggering of earthquakes. Bulletin of the Seismological Society of America 84, 935–953.
Klohn, C., 1960. Geologia de la Cordillera de los Andes de Chile Central, Provincia de Santiago, Colchagua y Curico, 8. Instituto de Investigaciones Geologicas Bulletin, Santiago, p. 95 (in Spanish).
Koerner, A., Kissling, E., Miller, S.A., 2004. A model of deep crustal fluid flow following the Mw= 8.0 Antofagasta, Chile, earthquake. Journal of Geophysical Research, Solid Earth 109 (B6). https://doi.org/10.1029/2003JB002816.
Lavenu, A., Cembrano, J., 1999. Compressional and transpressional-stress pattern for Pliocene and Quaternary brittle deformation in fore arc and intra-arc zones (Andes of Central and Southern Chile). Journal of Structural Geology 21, 1669–1691.
Leonard, M., 2010. Earthquake fault scaling: Self-consistent relating of rupture length, width, average displacement, and moment release. Bulletin of the Seismological Society of America 100 (5A), 1971–1988. https://doi.org/10.1785/0120090189.
Lin, J., Stein, R.S., 2004. Stress triggering in thrust and subduction earthquakes, and stress interaction between the southern San Andreas and nearby thrust and strike-slip faults. Journal of Geophysical Research 109, B02303. https://doi.org/10.1029/2003JB002607.
Lira, E., 2011. Estudio de Sismicidad, Tomografía Sísmica y Modelo de Física de Rocas: Potential Sistema Geotermal asociado al Complejo Volcánico Tinguiririca. Master Thesis. Energía Andina, Universidad de Chile, p. 189 (in Spanish with English abstract).
Lupi, M., Miller, S.A., 2014. Short-lived tectonic switch mechanism for long-term pulses of volcanic activity after mega-thrust earthquakes. Solid Earth 5 (1), 13–24.
Manga, M., Beresnev, I., Brodsky, E.E., Elkhoury, J.E., Elsworth, D., Ingebritsen, S.E., Mays, D.C., Wang, C.Y., 2012. Changes in permeability caused by transient stresses: field observations, experiments, and mechanisms. Reviews of Geophysics 50 (2), 1–24.
Marten, S.J., Boger, W.A., 1998. Geometry and mechanics of secondary fracturing around small three-dimensional faults in granitic rocks. Journal of Geophysical Research 103, 21299–21314.
Martínez-Dias, J.J., 2002. Stress field variation related to fault interation in a reverse oblique-slip fault: the Alhama de Murcia fault, Betic Cordillera, Spain. Tectonophysics 356, 291–305.
Meixner, J., Schill, E., Grimmer, J., Gaucher, E., Kohl, T., Klinger, P., 2016. Structural control of geothermal reservoirs in extensional settings: an example from the Upper Rhine Graben. Journal of Structural Geology 82, 1–15.
Mescua, J.F., 2011. Evolución estructural de la cordillera principal entre Las Choicas y Santa Elena (35° S), provincia de Mendoza, Argentina. PhD thesis. Universidad de Buenos Aires, p. 254 (in Spanish with English abstract).
Mescua, J.F., Giambiagi, L., Bechis, F., 2008. Evidencias de tectónica extensional en el Jurásico tardío (Kimeridgiano) del suroeste de la provincia de Mendoza. Revista de la Asociación Geológica Argentina 63 (4), 512–519 (in Spanish with English abstract).
Mescua, J.F., Giambiagi, L.B., Ramos, V.A., 2013. Late cretaceous uplift in the Malargüe fold-and-thrust belt (35 S), southern central Andes of Argentina and Chile. Andean Geology 40 (1), 102–116.
Mescua, J.F., Giambiagi, L.B., Tassara, A., Gimenez, M., Ramos, V.A., 2014. Influence of pre-Andean history over Cenozoic foreland deformation: structural styles in the Malargüe fold-and-thrust belt at 35°S, Andes of Argentina. Geosphere 10 (3). https://doi.org/10.1130/GES00939.1.
Micklethwaite, S., Cox, S.F., 2006. Progressive fault triggering and fluid flow in aftershock domains: examples from mineralized Archaean fault systems. Earth and Planetary Science Letters 250, 318–330.
Micklethwaite, S., Sheldon, H.A., Baker, T., 2010. Active fault and shear processes and their implications for mineral deposit formation and discovery. Journal of Structural Geology 32 (2), 151–165.
Miller, S., Collettini, C., Chiaraluce, L., Cocco, M., Barchi, M., Kaus, B., 2004. Aftershocks driven by a high-pressure CO2 source at depth. Nature 427, 724–727.
Moeck, I., Kwiatek, G., Zimmermann, G., 2009. Slip tendency analysis fault reactivation potential and induced seismicity in a deep geothermal reservoir. Journal of Structural Geology 31, 1174–1182.
Morris, A., Ferril, A., Henderson, D., 1996. Slip tendency analysis and fault reactivation. Geology 24, 275–278.
Mosolf, J., Gans, P.B., Wyss, A.R., Cottle, J.M., Flynn, J.J., 2018. Late Cretaceous to Miocene volcanism, sedimentation and upper-crustal faulting and folding inthe Principal Cordillera, central Chile: field and geochronological evidence for protracted arc volcanism and transpressive deformation. Geological Society of America Bulletin. https://doi.org/10.1130/B31998.1.

Muhuri, S.K., Dewers, T.A., Scott Jr., T.E., Reches, Z., 2003. Interseismic fault strengthening and earthquake-slip instability: friction or cohesion? Geology 31, 881–884.
Muñoz, M., Tapia, F., Persico, M., Benoit, M., Charrier, R., Farías, M., Rojas, A., 2018. Extensional tectonics during late cretaceous evolution of the southern central Andes: evidence from the Chilean main range at 35oS. Tectonophysics 744, 93–117.
Parada, R., 2008. Análisis estructural del borde oriental de la cuenca terciaria de Abanico en la valle del Río Teno, 7ma región. M.S. thesis. Universidad de Chile, p. 74 (in Spanish).
Pavez, C., Tapia, F., Comte, D., Gutierrez, F., Lira, E., Charrier, R., Benavente, O., 2016. Characterization of the hydrothermal system of the Tinguiririca Volcanic Complex, Central Chile, using structural geology and passive seismic tomography. Journal of Volcanology and Geothermal Research 310, 107–117.
Pineda, G., 2010. Geología del Proyecto Tinguiririca. Informe interno de Energía Andina S.A. (Unpublished).
Piquer, J., Castelli, J.C., Charrier, R., Yáñez, G., 2010. El Cenozoico del alto río Teno, Cordillera Principal, Chile Central: estratigrafía, plutonismo y su relación con estructuras profundas. Andean Geology 37, 32–53.
Reches, Z., 1978. Analysis of faulting in three-dimensional strain field. Tectonophysics 47, 109–129.
Rowland, J.V., Sibson, R.H., 2004. Structural controls on hydrothermal flow in a segmented rift system, Taupo Volcanic Zone, New Zealand. Geofluids 4 (4), 259–283.
Sheldon, H.A., Micklethwaite, S., 2007. Damage and permeability around faults: implications for mineralization. Geology 35, 903–906.
Sibson, R.H., 1977. Fault rocks and fault mechanisms. Journal of the Geological Society 133 (3), 191–213.
Sibson, R., 1990. Rupture nucleation on unfavorabley oriented faults. Bulletin of the Seismological Society of America 80, 1580–1604.
Sibson, R.H., 1996. Structural permeability of fluid-driven fault-fracture meshes. Journal of Structural Geology 18, 1031–1042.
Sibson, R.H., Rowland, J.V., 2003. Stress, fluid pressure and structural permeability in seismogenic crust, North Island, New Zealand. Geophysical Journal International 154, 584–594.
Siler, D.L., Faulds, J.E., Hinz, N.H., 2015. Earthquake-related stress concentrations and permeability generation in geothermal systems. GRC Transactions 39, 437–444.
Spagnotto, S., Triep, E., Giambiagi, L., Lupari, M., 2015. Triggered seismicity in the Andean arc region via static stress variation by the Mw=8.8, February 27, 2010, Maule Earthquake. Journal of South American Earth Sciences 63, 36–47.
Stein, R.S., 1999. The role of stress transfer in eearthquake occurrence. Nature 402, 605–609.
Tapia, F., Farías, M., 2011. Análisis est ructural del sector Occidental de la faja plegada y corrida de Malargüe en el área de Valle Grande, Región del Maule, Chile (35o23'S). In: 18o Congreso Geologico Argentino, Neuquen, p. 895 (in Spanish).
Tapia, F., Farías, M., Naipauer, M., Puratich, J., 2015. Late Cenozoic contractional evolution of the current arc-volcanic region along the southern Central Andes (35°20'S). Journal of Geodynamics 88, 36–51.
Tezuka, K., Niitsuma, H., 2000. Stress estimated using microseismic clusters and its relationship to the fracture system of the Hijiori hot dry rock reservoir. Engineering Geology 56, 47–62.
Toda, S., Stein, R., Richards-Dinger, K., Bozkurt, S., 2005. Forecasting the evolution of seismicity in southern California: animations built on earthquake stress transfer. Journal of Geophysical Research 110 (B5), B05S16.
Townend, J., Zoback, M.D., 2000. How faulting keeps the crust strong. Geology 28, 399–402.
Twiss, R.J., Moores, E.M., 1992. Structural Geology. Macmillan.
Twiss, R.J., Unruh, J.R., 1998. Analysis of fault slip inversions: do they constrain stress or strain rate? Journal of Geophysical Research 103 (12), 205-12,222.
Vergani, G., Tankard, A.J., Bellotti, H., Welsink, H., 1995. Tectonic evolution and paleogeography of the Neuquén basin, Argentina. In: Tankard, A.J., Suárez, R., Welsink, H.J. (Eds.), Petroleum Basins of South America, vol. 62. AAPG Memoir, pp. 383–402.
Vicente, J.C., 2005. Dynamic paleogeography of the Jurassic Andean Basin: pattern of transgression and localisation of main straits through the magmatic arc. Revista de la Asociación Geológica Argentina 60 (1), 221–250.
Villegas, A., Raquel, J., Zahradnik, J., Nacif, S., Spagnotto, S., Winocur, D., Flavia Leiva, M., 2016. Waveform inversion and focal mechanisms of two weak earthquakes in Cordillera Principal (Argentina) between 35 degrees and 35.5 degrees S. Journal of South American Earth Sciences 71, 359–369.
Walsh, J.B., Grosenbaugh, M.A., 1979. A new model for analysing the effect of fractures on compressibility. Journal of Geophysical Research 84, 3532–3536.
Wells, D.L., Coppersmith, K.J., 1994. New empirical relationships among magnitude, rupture length, rupture width, rupture area, and surface displacement. Bulletin of the Seismological Society of America 84 (4), 974–1002.
Wicks, C., de La Llera, J., Lara, L., Lowenstern, J., 2011. The role of dyking and fault control in the rapid onset of eruption at Chaitén volcano, Chile. Nature 478, 374–377.
Zalohar, J., Vrabec, M., 2007. Paleostress analysis of heterogeneous fault-slip data: the Gauss method. Journal of Structural Geology 29, 1798–1810.
Zapatta, F., 1995. Nuevos antecedentes estratigráficos y estructura del área de Termas del Flaco, valle del río Tinguiririca, VI Región, Chile. M.S. Thesis. Universidad de Chile, p. 122 (in Spanish).
Zoback, M.D., Townend, J., 2001. Implications of hydrostatic pore pressures and high crustal strength for the deformation of intraplate lithosphere. Tectonophysics 336, 19–30.